Deciphering the Ultra-High Plasticity in Transition Metal Monochalcogenides

Lok Wing Wong[1,2,†], Ke Yang[1,2,†], Wei Han[1,2], Xiaodong Zheng[1,2], Hok Yin Wong[1,2], Chi Shing Tsang[1,2], Chun-Sing Lee[3], Shu Ping Lau[1], Thuc Hue Ly[3,4,5,*], Ming Yang[1,2,*] & Jiong Zhao[1,2,6*]

[1] Department of Applied Physics, The Hong Kong Polytechnic University, Kowloon, Hong Kong, China
[2] Polytechnic University of Hong Kong Shenzhen Research Institute, Shenzhen, China.
[3] Department of Chemistry and Center of Super-Diamond & Advanced Films (COSDAF), City University of Hong Kong, Kowloon, Hong Kong, China
[4] Department of Chemistry and State Key Laboratory of Marine Pollution, City University of Hong Kong, Hong Kong, China
[5] City University of Hong Kong Shenzhen Research Institute, Shenzhen, China
[6] The Research Institute for Advanced Manufacturing, The Hong Kong Polytechnic University.

*Email: jiongzhao@polyu.edu.hk (J.Z.), kevin.m.yang@polyu.edu.hk (M.Y.), thuchly@cityu.edu.hk (T.H.L.)
†These authors contribute equally.

Abstract

The quest for electronic devices that offer flexibility, wearability, durability, and high-performance, while simultaneously exploring new additive manufacturing technologies to enhance the plasticity and elasticity of inorganic semiconductors, has spotlighted two-dimensional van der Waals (vdW) materials as potential next-generation semiconductors. Especially noteworthy is indium selenide (InSe), which has demonstrated surprising ultra-high plasticity. The recent achievement of a high-performance ballistic transistor utilizing 2D InSe has further sparked considerable interest. In an effort to deepen our understanding of this unusual plasticity in 2D vdW materials and to explore additional inorganic plastic semiconductors, we have conducted in-depth experimental and theoretical investigations on MX (M = In, Ga; X = S, Se, Te) and MX_2 (M = Mo, W; X = S, Se, Te) vdW layered materials. We have discovered a novel and general plastic deformation mode in MX materials, which is facilitated by the synergetic effect of phase transitions, inter-layer gliding, and microcracks. This is in contrast to crystals with strong atomic bonding, such as metals and ceramics, where plasticity is primarily driven by dislocations. Via atomic-scale transmission electron microscopy, *in situ* experiments, first-principles calculations, and molecular dynamics simulations, we have unveiled that the key to generating numerous microcracks in a well-synchronized manner, while avoiding crack coales-

cence, growth, or macroscopic fracture, is the facile phase transitions associated with switchable stacking order and increased interlayer gliding barriers resulting from the 2H-to-3R phase transition in MX, but not in MX_2. By harnessing the 3R pinning effect, it is possible to cease the propagation of microcracks, resulting in enhanced deformability. The discovery of ultrahigh plasticity and the novel phase transition mechanism combining microcrack deformation found in 2D MX materials, could be useful for the design and the development of high-performance inorganic plastic semiconductors.

Introduction

Writing with a pencil involves the mechanical deformation of graphite on the pencil tip through compression and lateral friction, which is then transferred to paper and forms a thin film. At the microscopic level, numerous fracture events occur on the tip during this process. For “3H” or “2H” grading pencils[1,2], the lack of plastic deformation on the tip results in discontinued patterns and lighter-colored writing. In contrast, softer “3B” or “2B” grading pencils can create much smoother and continuous writing due to their improved plasticity. The hardness and plasticity of the pencil tips are essentially determined by the structure and compositions of the materials[1,2].

Similar to graphite, a rich family of van der Waals (vdW)-layered materials have been known for their strong intralayer bonding and weak interlayer interaction, which makes them easy to exfoliate into the atomically-thin two-dimensional (2D) films[3-8]. Ultra-thin metal chalcogenides (MX: M = Ga, In; X = S, Se, Te)[9-14] and transition metal dichalcogenides (TMDCs, MX_2: M = Mo, W; X = S, Se, Te)[15-23]possess attractive properties such as high carrier mobility[12-14,22,23], high on/off ratio[12-16], low subthreshold swing[14,15,20], high deformability[7,8,13,15,19,24-26], and ferroelectricity[27,28]. Very recently, an InSe-based ballistic 2D transistor was reported to outperform Si-based FinFETs in terms of higher room temperature ballistic ratio, lower working voltage, lower power consumption, and smaller delay[14]. Surprisingly, InSe has demonstrated remarkably high plasticity, which is in contrast with other vdW-layered materials that prevalently consist of brittle covalent and ionic bonding[7,8]. Benefiting from the intrinsic 2D semiconducting properties, and the ultra-high deformation capabilities with significantly lowered fracture and fragmentation tendencies, this type of vdW-layered materials, especially the MX, hold promising potentials for future flexible electronics[13,24,29], as well as wearable and bio-compatible devices[24,26]. Moreover, the facile interlayer gliding ensures ultra-low friction between layers, enabling the vdW-layered materials to serve as solid-state lubricants (SSL) in industrial and engineering fields[30-32], as well as in additive manufacturing[33] and 3D printing[34,35] technologies for next-generation inorganic semiconductors.

In terms of plasticity, InSe, GaSe, and MoS_2 have exhibited the ability to sustain tensile fracture strains along basal plane up to ~12%, ~11%, and ~9%, respectively, and all of these materials can be deformed over 20% bending strain[7,8]. Apparently, this ultra-high plasticity is associated with the interlayer gliding. In addition, the role of the cross-layer dislocation slip has been addressed due to the synergistic effect of interlayer interactions and high cleaving energy[7]. However, the full picture of the plastic deformation in vdW layered materials, especially why the quadruple-layered MX (such as InSe and GaSe) possesses better deformability than other vdW-layered materials such as graphite[36,37] and TMDCs like MoS_2[7,8] is not yet clear.

Here, we perform comprehensive structural analysis at the atomic scale by scanning transmission electron microscopy (STEM), particularly the *in situ* TEM, combined with first-principles calculations and molecular dynamics (MD) simulations to investigate the structural evolution during the plastic deformation of various vdW-layered materials. We find that there are high density micro-cracks and phase transition after applying mechanical loading, which effectively relieve the strain and are responsible for the ultrahigh plasticity. The stacking order-relevant phase transition has been overlooked in the previous experimental and theoretical studies[7,8,38]. Besides, the interlayer gliding barriers show stark difference between 2H and 3R stacking orders, creating pinning points which cease the continuous crack propagation and the subsequent catastrophic failure.

Emergent polymorphs by mechanical deformation

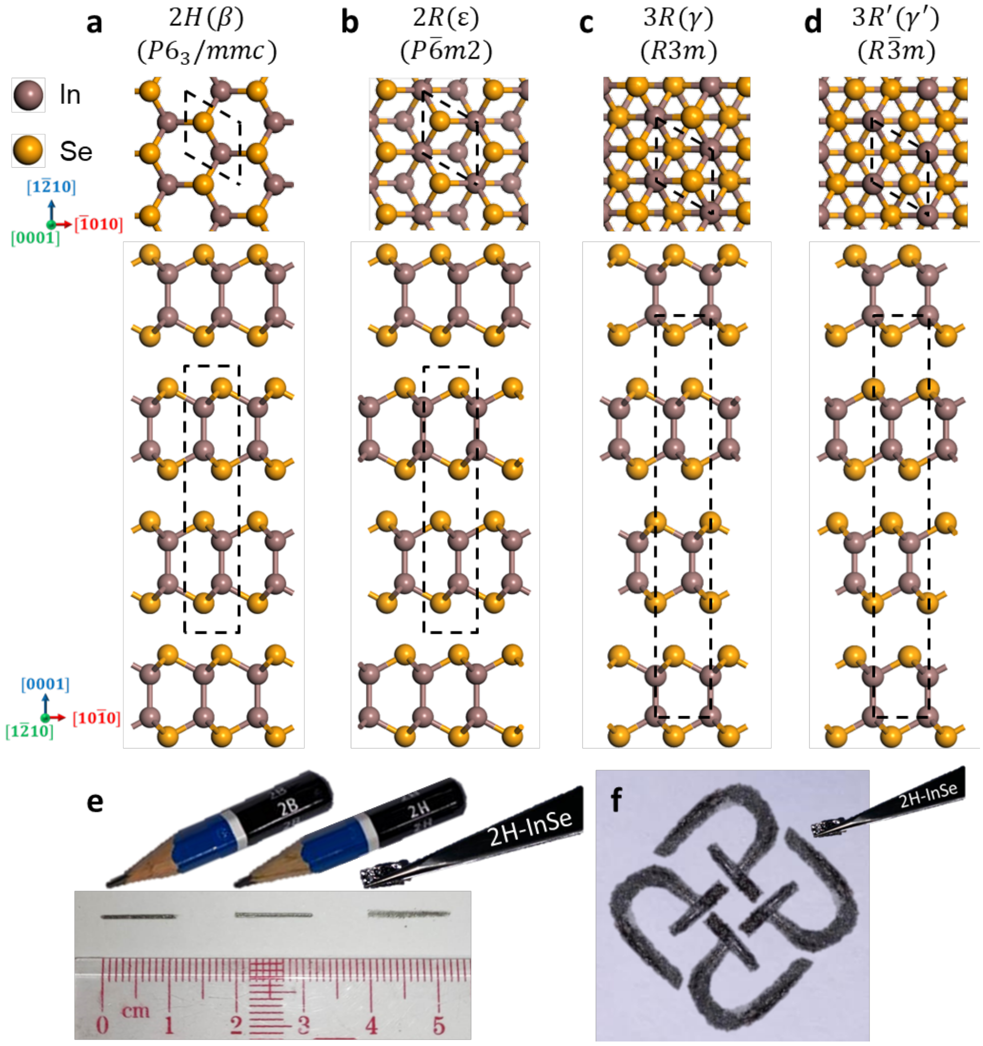

Fig. 1 | Atomic structures of various InSe phases (top and cross-section views) and writing capability as a pen. a-d, Atomic structures of 2H-InSe (**a**), 2R-InSe (**b**), 3R-InSe (**c**), and 3R'-InSe (**d**). Unit cells are indicated by the black dashed boxes. **e-f,** Drawing ability of pristine 2H-InSe demonstrated by drawing a straight line compared with 2B and 2H pencils (**e**), and a PolyU logo written by the pristine 2H-InSe crystal (**f**).

InSe is primarily composed of four phases: 2H(β)-InSe (space group: $P6_3/mmc$) is also called 2H phase, whereas the adjacent atomic layers are twisted by 60° (equivalent to 180°)[39]; the counterpart 2R(ε), 3R(γ), and 3R'(γ')-InSe (space group: $P\bar{6}m2$, $R3m$, and $R\bar{3}m$, respectively) are all stacked without twisting (Fig. 1a-d). The other MX materials, such as GaSe, exhibit similar polymorphic structures as InSe[40]. First, we showcase the macroscopic ultra-high plasticity in 2H-InSe by direct writing and drawing with the 2H-InSe crystal. As shown in Fig. 1e, the 2H-InSe crystal shows good writing capability that is comparable with that of 2B and 2H pencils. This can be further seen from the PolyU logo (Fig.1f) drawn by the 2H-InSe crystal. The capability of 2H-InSe for continuous writing and patterning is comparable to that of graphite pencils, highlighting its immense potential for future additive manufacturing applications, particularly in the realm of next-generation 2D semiconductors. Examples of these applications include the use of InSe ink for 3D printing or as a drawing pen for 2D semiconductors, and even as a fundamental component in the development of flexible electronics.

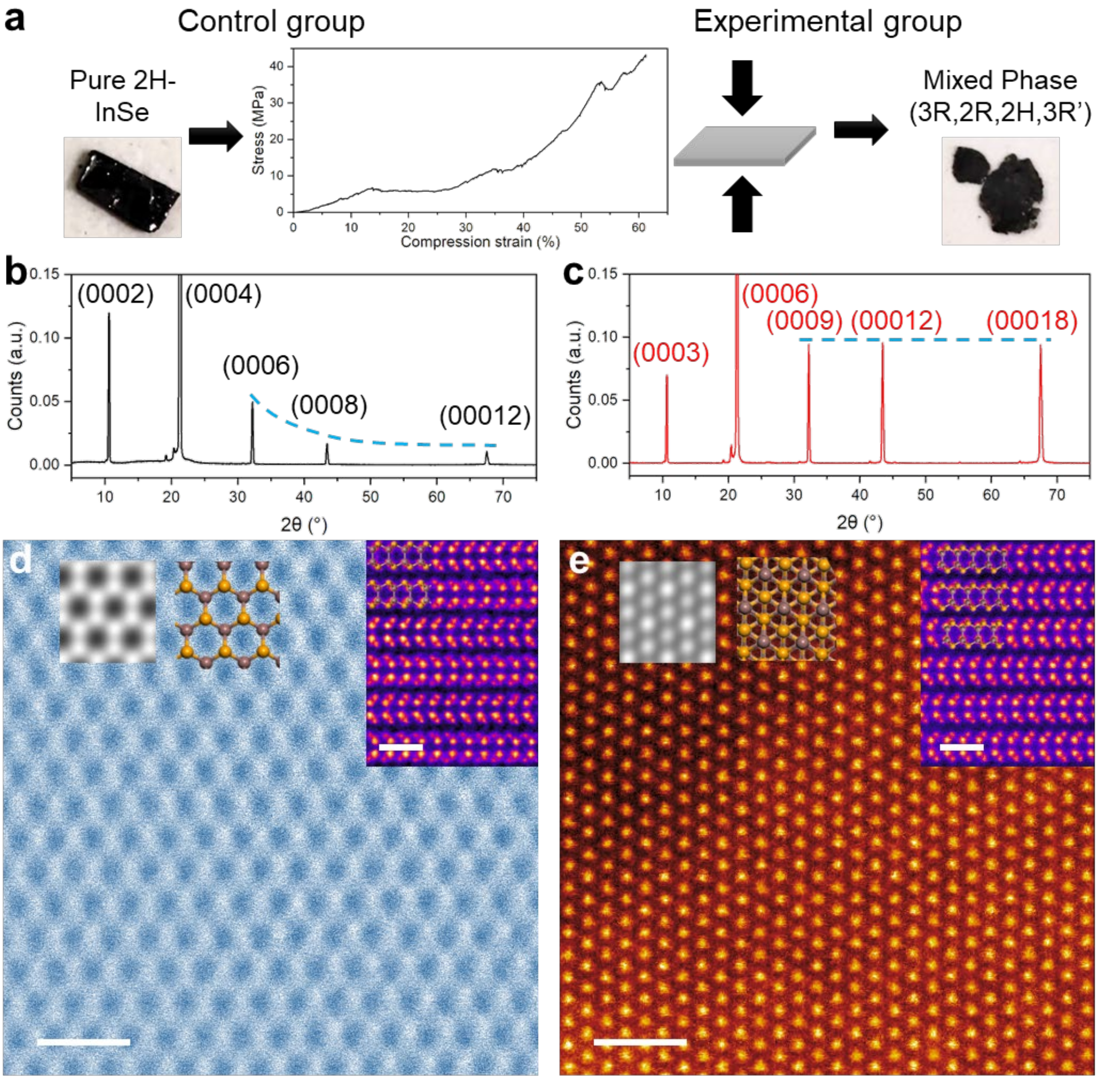

Fig. 2 | The structural evolution of 2H-InSe after mechanical deformation. a, The experimental workflow. **b,c,** XRD results of control group (before deformation) (**b**), and experimental group (after deformation) (**c**). The light blue dashed lines highlight the differences between (**b**) and (**c**). **d,e,** High resolution STEM-HAADF images in zone axis of [0001] and $[1\bar{2}10]$ of the control group (**d**), and the experimental group (**e**), showing 2H and 3R stacking, respectively. Insets in (**d**,**e**), STEM simulation images (details see Method). Scale bars: 1 nm.

In following experiments, the single crystal 2H-InSe, 2H-GaSe, 2H-MoS_2, and 2H-$MoTe_2$ were mechanically compressed as shown in Fig. 2a (see Methods for details). The intralayer strain provided by compression on the single crystals, including 2H-InSe, 2H-MoS_2 and 2H-$MoTe_2$, results in significant plastic deformation over 40% compression strain (Supplementary Fig. S1), until the limitation of the machine. While a few macroscopic cracks were generated, the majority of the samples remained continuous and preserved in one piece. The crystal stacking of pristine InSe and post-deformed InSe, MoS_2 and $MoTe_2$ exhibit consistent and high-quality characteristics on a large scale, as demonstrated and arranged in Supplementary Fig. S2-S10, showcasing both the [0001] top and $\langle 1\bar{2}10 \rangle$ cross-section views.

The compression tests successfully induced micro-cracks and plastic deformation within the InSe crystals. A comparison of the X-ray diffraction (XRD) results of pre-deformation and post-deformation InSe, as shown in Figs. 2b-c respectively, reveals distinct signatures of phase transition indicated by the noticeable change in peak ratios marked by the light blue dashed lines. In contrast, the millimeter-scale XRD results of MoS_2 and $MoTe_2$, as depicted in Supplementary Fig. S11, do not exhibit significant shifts or changes in peak intensity. The pristine 2H-InSe single crystal undergoes a transformation into InSe polymorph, primarily in the 3R phase, as depicted in Figs. 2b-e. Remarkably, this observed phase transition is solely induced by mechanical force, differing from the thermal treatments commonly reported in the literature[18,41-43]. The top view and cross-section scanning transmission electron microscopy high-angle annular dark-field (STEM-HAADF) images exhibit excellent agreement with the XRD results (Figs. 2b-e). In the control group, pristine samples display a clean 2H stacking represented by the blue color scale, while the experimental group subjected to plastic deformation exhibits a 3R stacking represented by the orange color scale. The STEM-HAADF images for both phases align with their corresponding atomic models and the STEM-HAADF simulation, as illustrated in Figs. 2d-e. The top view STEM-HAADF results also provide sufficient information of the pristine 2H stacking and post-deformed 3R stacking, as shown in Supplementary Fig. S12.

Meanwhile, our Raman spectroscopy data does not show extra peak for pre-deformation and post-deformation InSe with respect to control and Exp. 1-3, respectively (Extended Data Fig. 1). Exps. 1-4 refer to the same batch of exfoliated InSe after loading with different laser exciting positions, indicated by the orange crosses. It can be distinguished by the peak ratios of $E'(1)$ and $E''(2)$. $E'(1)$ peak is higher than $E''(2)$ peak when the InSe is generally 3R stacking, while those two peaks are similar indicating the InSe is 2H stacking. However, only the red dashed box in Exp. 4 displays a red shift with an extra peak that attributes to some local 2R phase, which can be recognized as the stacking faults in 3R phase[41,42], and it is also verified by the cross-section STEM results (Supplementary Fig. S13). On the other hand, Supplementary Figs. S14-S15, the post-deformation MoS_2 and $MoTe_2$ behave the same A_{1g} and E_{2g} in Raman shift compared with their pre-deformation results, that suggest no phase transition occur after compression.

The corresponding low magnification TEM and diffraction patterns of Figs. 2d&e are shown in Extended Data Figs. 2&3. The diffraction patterns of the pristine InSe demonstrate stronger $\{1\bar{2}10\}$ signals highlighted by the yellow circles, while the post-deformation InSe displays similar intensity. From the cross-section views, the post-deformed InSe exhibits a shorter interlayer distance and displays splitting diffraction patterns, specifically marked as $(10\bar{1}1)$ and $(10\bar{1}2)$, indicating the presence of mixed phases, predominantly 3R, in the post-deformed InSe. Based on these characterizations, it can be concluded that the post-deformed InSe generally exhibits a 3R stacking configuration. Extended Data Fig. 4 presents typical low magnification STEM-HAADF (top views) after deformation. InSe demonstrates a tendency to form numerous intralayer micro-cracks, with fewer dislocation lines and more pronounced fractures compared to MoS_2 and $MoTe_2$. Conversely, Extended Data Fig. 5 showcases typical low magnification STEM-HAADF cross-section views. The micro-cracks in InSe are relatively discrete and propagate along the basal plane, while in MoS_2 and $MoTe_2$, the micro-cracks prefer continuous propagation and have a higher likelihood of propagating through interlayers, particularly evident in Extended Data Figs. 5f,h&i. These results indicate that InSe can effectively relief strain by forming micro-cracks associated with phase transition, distinguishing it from the behavior of MoS_2 and $MoTe_2$.

The distribution and propagation of micro-cracks in InSe, MoS_2, and $MoTe_2$ highlight the significance of phase transition in determining their plasticity. The presence of well-developed micro-crack networks in deformed InSe suggests that strain concentration is evenly distributed. Consequently, the strain is continuously relaxed through interlayer gliding with free ends at the micro-cracks. In contrast, MoS_2 and $MoTe_2$ tend to accumulate dislocations. When the strain becomes unsustainable, severe fracture occurs as a catastrophic means of strain relaxation. As explained in detail below, the previously unreported mechanically driven phase transition of MX plays a crucial role in the generation and propagation of micro-cracks.

The atomic structures near the micro-cracks

After the large-scale characterizations, the atomic structures near micro-cracks, created under deformation, are investigated in detail below. In comparisons among InSe, MoS_2 and $MoTe_2$

specimens, Fig. 3a-c show the atomic structure near the micro-cracks. The pristine 2H-InSe transforms to mainly 3R phase, but MoS_2 and $MoTe_2$ retain 2H phase (detailed structural models of MX and MX_2 can be seen in Supplementary Fig. S16). The large field of view insets present the corresponding position of the atomic STEM-HAADF highlighted by the orange dashed boxes. More positions from a ~13 μm post-deformation InSe cross-section also provide wide range of the 3R stacking domination near the micro-cracks, as shown in Extended Data Fig. 6. In panel f, green, yellow, and blue color highlight the 3R' stacking, phase boundary, and 2H stacking, respectively. On the other hand, clear 2H-stacking with some lattice damage can be observed in the post-deformed MoS_2 and $MoTe_2$ near the micro-cracks and defects, as shown in Extended Data Figs. 7&8, respectively. The results agree with the large-scale results that phase transition occurred in InSe, but not in MX_2.

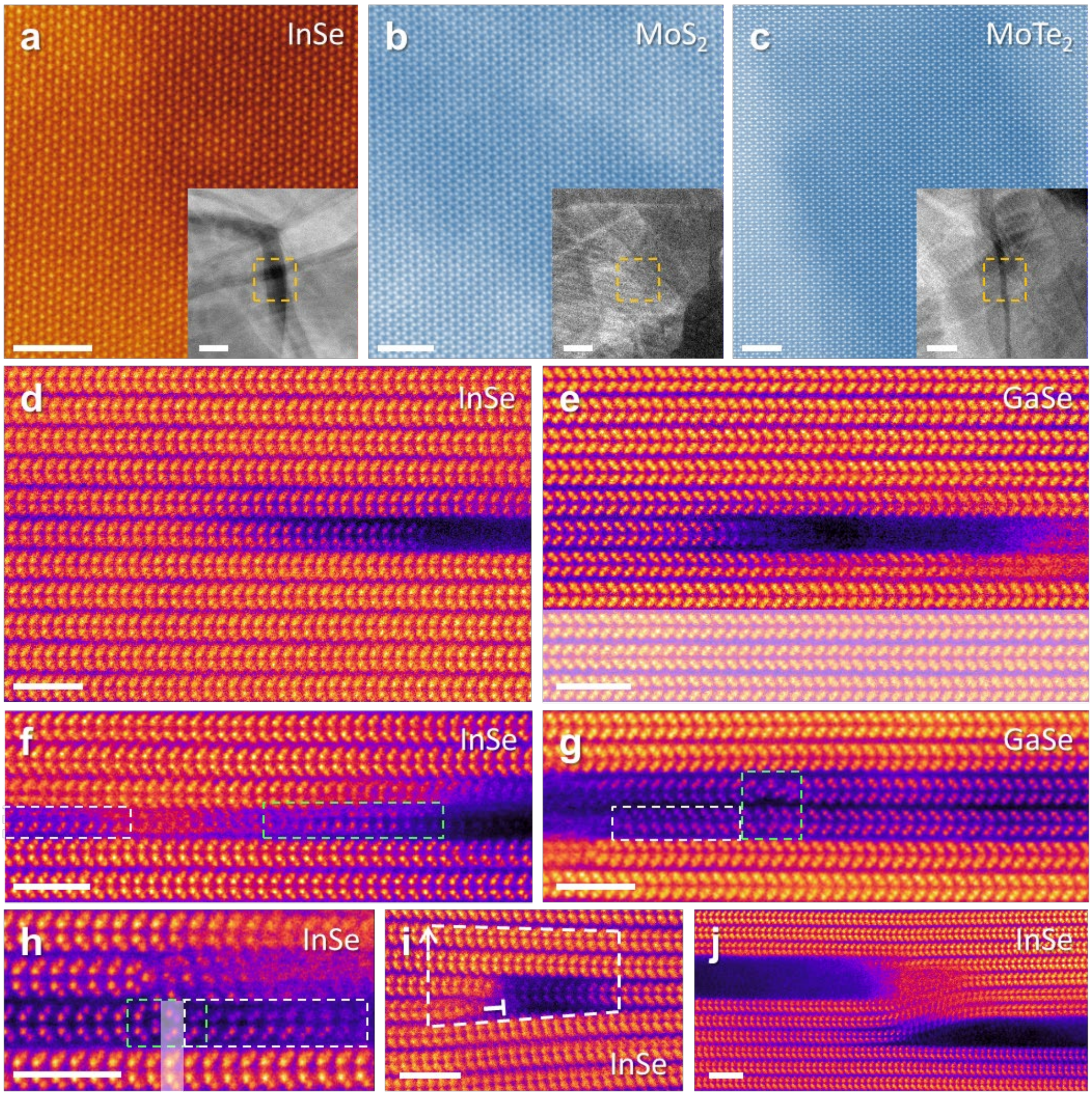

Fig. 3 | Atomic structures near micro-cracks. a-c, Atomic images near micro-cracks of InSe (**a**), MoS_2 (**b**), and $MoTe_2$ (**c**) along [0001]. The insets in (**a-c**) with 50 nm scale bars show the corresponding position in (**a-c**) highlighted by orange dashed boxes. The orange and blue color scale represent 3R and 2H stacking in (**a-c**), respectively. **d-j,** Cross-section STEM-HAADF images of InSe and GaSe along $[1\bar{2}10]$. **d**,**e**, A typical micro-crack in InSe (**d**) and GaSe (**e**) after deformation. **f-h,** Mechanical force driven intralayer phase boundaries (highlighted by green dashed boxes) with intermediate 3R' stacking (highlighted by white dashed boxes) in InSe (**f,h**) and GaSe (**g**). The white area in (**e,g,h**) highlights the untransformed 2H stacking. **i,** One micro-crack forms $1/3z$ edge dislocation. **j,** A cross-layer joint of two micro-cracks. Scale bars: 2 nm (**a-j**).

We further zoom into the micro-cracks and dislocations in Figs. 3d-j for investigations. Fig.3d,e display STEM images of a typical single layer (1L) micro-crack of InSe and GaSe surrounded mainly by 3R stacking, whereas only 1L breaks without forming dislocations (larger field of view can be seen in Supplementary Figs. S17&S18). In Fig. 3e, the post-deformed GaSe without phase transition is also highlighted in white, showing 2H stacking. Similarly, the typical few layers micro-cracks of InSe and GaSe are also surrounded by mainly 3R stacking (Extended Data Fig. 9). These cross-section STEM results are in line with the above analysis that more 3R stacking is formed after mechanical deformation.

With careful inspection on the post-plastic-deformation InSe and GaSe specimens, Fig. 3f-h capture more atomic signatures about the phase transitions and the phase boundaries. Particularly, the 3R/2H/3R' phase boundaries and 3R'-MX are indicated by the green and white dashed boxes, respectively. The untransformed 2H-MX and completely transformed 3R-MX are found with the 3R'-MX near 3 different bilayer micro-cracks. The results imply that 3R'-MX can be as an intermediate stage of phase transition pathway from 2H to 3R caused by intralayer atomic reconstruction. This intermediate stage can reduce the energy requirement for phase transition. C-BN-to-r-BN-to-h-BN phase transition is a good example, that shows the 2-step phase transition is more energy favorable than direction phase transition of c-BN-to-h-BN[43,44]. We believe that the energy favorable 2-step phase transition allows MX to afford more strain and to achieve better plasticity.

From a structural perspective, the emerged 3R-InSe cannot be simply caused by interlayer gliding along the energy favorable axis such as $\langle 10\bar{1}0\rangle$ or $\langle 1\bar{2}10\rangle$. Instead, the intralayer reconstruction is necessary. According to our density functional theory (DFT) calculations, the formation energy of 2H and 3R phase is very close, -0.755, and -0.756 eV/atom (Extended Data Table 1), respectively, which explains the co-existed phases as observed (Figs. 3a,d,f&h). The slightly lower energy in 3R phases also implies a stronger inter-layer interaction in 3R phase than 2H phase, which is also in agreement with exfoliation energy difference for the two phases (0.27, and 0.29 J/m^2 for 2H and 3R phase, respectively).

It can be rationalized that the formation of micro-cracks is much easier at the high energy phase boundaries. Then, a two-step phase transition from 2H-to-3R'-to-3R was calculated in this phase boundary model. The results suggest that 2H phase can transform to 3R' phase (Step 1 to Step 2) as indicated by a relatively low energy barrier of 0.275 eV. At the end, the transition from 3R' to 3R phase (Step 2 to Step 3) can reach a lower energy, which is lower than Step 1 by ~1.5 meV (Supplementary Fig. S19). These results suggest that the 3R' stacking can serve as the intermediate state by allowing the translation of the Se atom one by one during mechanical deformation, and the lower relaxation energy in 3R phase than 2H phase suggests that 3R phase is more energy favorable under mechanical deformation in MX. A similar observation is made in GaSe (Fig. 3e,g)

Moreover, other than the phase boundary induced micro-cracks, edge dislocations like $\boldsymbol{b} = 1/3\boldsymbol{z}$ can also initiate micro-cracks at the high energy zones (Fig. 3i). Extended Data Fig. 10 presents the geometric phase analysis results of the 3R region without micro-crack, the phase boundary and the $1/3\boldsymbol{z}$ edge dislocation. The phase boundary and the edge dislocation are highly strained area incubating micro-cracks. After prevailed micro-crack generation, the suddenly ceased extension of these micro-cracks is owing to the higher energy barrier for the gliding in 3R stacking than original stacking (see later discussion).

Interestingly, Fig. 3j demonstrates that the micro-cracks in different layers can combine and automatically stop the propagation of each other. Usually, coalescence of cracks will bring catastrophic failure, but in InSe and GaSe, the micro-cracks in different layers can self-collectively form a stable network. Fig.3j shows that a cross-layer joint of two micro-cracks connecting 3L InSe prevents micro-cracks further propagation. Until now, we have clarified that the correlated micro-cracks and phase transition are the key to the high plasticity of MX, which is in contrast with other brittle vdW layered materials.

Mechanical manipulations by *in situ* TEM method

In order to gain deep insight into the plastic deformation of MX, *in situ* TEM bending experiments were implemented with exfoliated 2H-InSe (Fig. 4). We expect that plastic deformation could occur in those highly bended zones. Herein, Figs. 4a-c demonstrate that an InSe flake with dislocation lines is bent by the nanomanipulator with a tungsten tip inside TEM (Methods). Two emerged dislocation lines are tracked by the white and red arrows. One crack is initiated at the dislocation position marked by the white arrows. The intralayer micro-cracks are obviously created by the concentrated strain. Notably, the bending induced interlayer gliding can also eliminate the dislocation traced by the red arrows in Figs. 4a&b. The strain is prone to be relaxed by the phase transition and interlayer gliding facilitated by numerous discontinuous micro-cracks along basal plane rather than combining or extending the micro-cracks across different layers as the comparison of post-deformation specimen in STEM-HAADF in Extended Data Figs. 2-8. On the other hand, another cross-layer joint is found in Fig. 4c, as highlighted by the green dashed box, which is similar to the case in Fig. 3j. The thickness of the intralayer micro-cracks can be a 4L micro-crack or a pair of 2L micro-cracks indicated by the white arrows in Figs. 4b&c. The thickness of the intralayer cracks that continuously fracture along *z* direction can be defined by the layer numbers, which can be determined by the contrast in STEM-HAADF images under the same imaging condition (Methods, Fig. 4c and Supplementary Fig. S20). The thickness estimated by STEM-HAADF intensity is similar to the one used in the previous study[45]. An outmost fracture labeled by green dashed line is created during the *in situ* bending (Supplementary Video 1). Thus, here we further show that the propagation of micro-cracks can be stopped when they meet, therefore numerous nanometer (nm)-width micro-cracks without further expansion in InSe can be clearly seen in low magnification STEM-HAADF (Extended Data Fig. 4b).

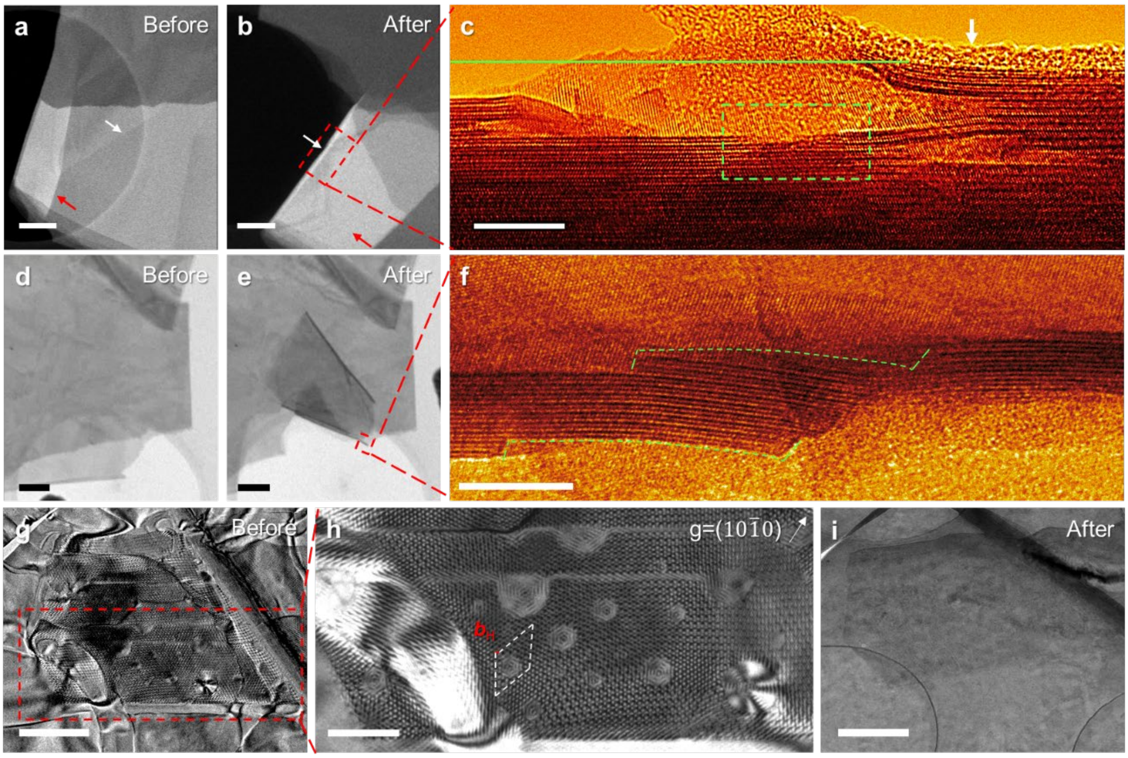

Fig. 4 | *In situ* TEM experiments of InSe. a-c, STEM-HAADF images before (**a**), and after (**b**) *in situ* bending experiment with corresponding HRTEM image (**c**) indicated by the red dashed box in (**b**). An outermost fracture during *in situ* bending experiment is indicated by green line (Supplementary Video 1) and a cross-layer joint of micro-cracks is highlighted by the green dashed box. The white arrows and red arrows denote two dislocations in (**a-c**). **d-f**, Another set of *in situ* bending experiment. Snapshots before (**d**) and after (**e**) *in situ* experiment with corresponding HRTEM image (**f**) indicated by the red dashed box. A pair of green dashed lines indicate the original position of the edges before vertical fracture in (**h**). **g-i**, TEM images of hyperdislocation networks with disregistry before (**g,h**) and after (**i**) *in situ* shear experiment of a deformed InSe. **h,** DF TEM image indicated by the red dashed box in (**g**); g = $(10\bar{1}0)$ with an example of the Burgers vector of the edge hyperdislocations $\boldsymbol{b}_H$ =

$\sqrt{3}\lambda/3[0\bar{1}10]$ denoted by white dashed loop with red arrow. The Scale bars: 200 nm (**a**,**b**,**d**,**e**,**h**), 10 nm (**c**,**f**), and 500 nm (**g**,**i**).

Achieving excellent compression ratio (>4000%[7]) needs to reduce the number of layers of vdW materials without macroscopic fracture. The secret for preventing complete interlayer fracture is uncovered by our *in situ* TEM, that InSe re-attaches not only with the adjacent interlayer, but also easily with the completely fractured parts (Figs. 4d-f). In Fig. 4f, the cross-section view shows the fractured area recovers by re-attachment, highlighted by a pair of green dashed lines (details see Supplementary Fig. S21). The slightly stronger interfacial energy here contributes to the stability of the layered structure during the lateral expansion of micro-cracks, and upon gliding, the newly extracted layers are able to keep the integrity of the structure.

In the third *in situ* experiment shown here, the dislocation networks in pre-deformed InSe caused by layer twisting under deformation can be observed in a local area in Figs. 4g-i, with some hyper-dislocations same as the observation in $MoTe_2$ in our previous report[46]. Here we found, in MX materials, the density of hyperdislocations is significantly higher, which may be linked to the enhanced tendency for partial layer cleavage and reconnection observed in InSe and other MX materials, which well preserved the overall structure without fracture. The period of the superlattice is denoted as λ. Same full (edge) dislocation can be found from the hyper-dislocation area with disregistry with the hyper-dislocation Burgers vector $\boldsymbol{b}_H = \sqrt{3}\lambda/3[0\bar{1}10]$ as shown in the dark-field (DF) TEM image in Fig. 4h. These hyper-dislocations are basically caused by some in-plane defects, such as phase boundaries and micro-cracks which have been elaborated above. Furthermore, after more shear stress is applied on this sample by the tungsten tip mounted on the nanomanipulator, the ease of interlayer gliding and the intra- and inter-layer crack healing effect as mentioned above can significantly reduce the defect densities, and the dislocation network also vanishes due to restored layer stacking registry.

Phase transition barrier and interlayer gliding barrier

In order to examine the physical origin which prevents the interlayer propagation of micro-cracks in 2H-InSe and the contribution of the phase transition, we have performed in-depth first-principles calculations and molecular dynamics (MD) simulations by comparing MX and MX_2 in Fig. 5. First, the first-principles calculations were used to evaluate the bonding strength, phase transition energy, and gliding energy of 2H and 3R stacking along $\langle 10\bar{1}0\rangle$ armchair and $\langle 1\bar{2}10\rangle$ zigzag direction of the representatives of MX and MX_2 (InSe and MoS_2), as shown in Figs. 5a-d. It is noted that the phase transition requires lattice rotation or X atom translation. Without thermal treatment, X atom translation is preferred under deformation, and each translation requires breaking one intralayer M-X bond and translating a X atom along $1/3\langle 10\bar{1}0\rangle$.

Their relative bonding energies are examined in Figs. 5a&b by crystal orbital Hamilton populations (COHP) (Methods, more comparison see Supplementary Fig. S22). The bonding strength of In-Se (~3.855 eV/bond) is found weaker than that of Mo-S (~4.368 eV/bond). These results imply the breaking of intralayer In-Se bond in InSe is relatively easier than breaking of intralayer Mo-S bond in MoS$_2$, which facilitates the movement of X atoms in MX, and eventually the change of atomic stacking.

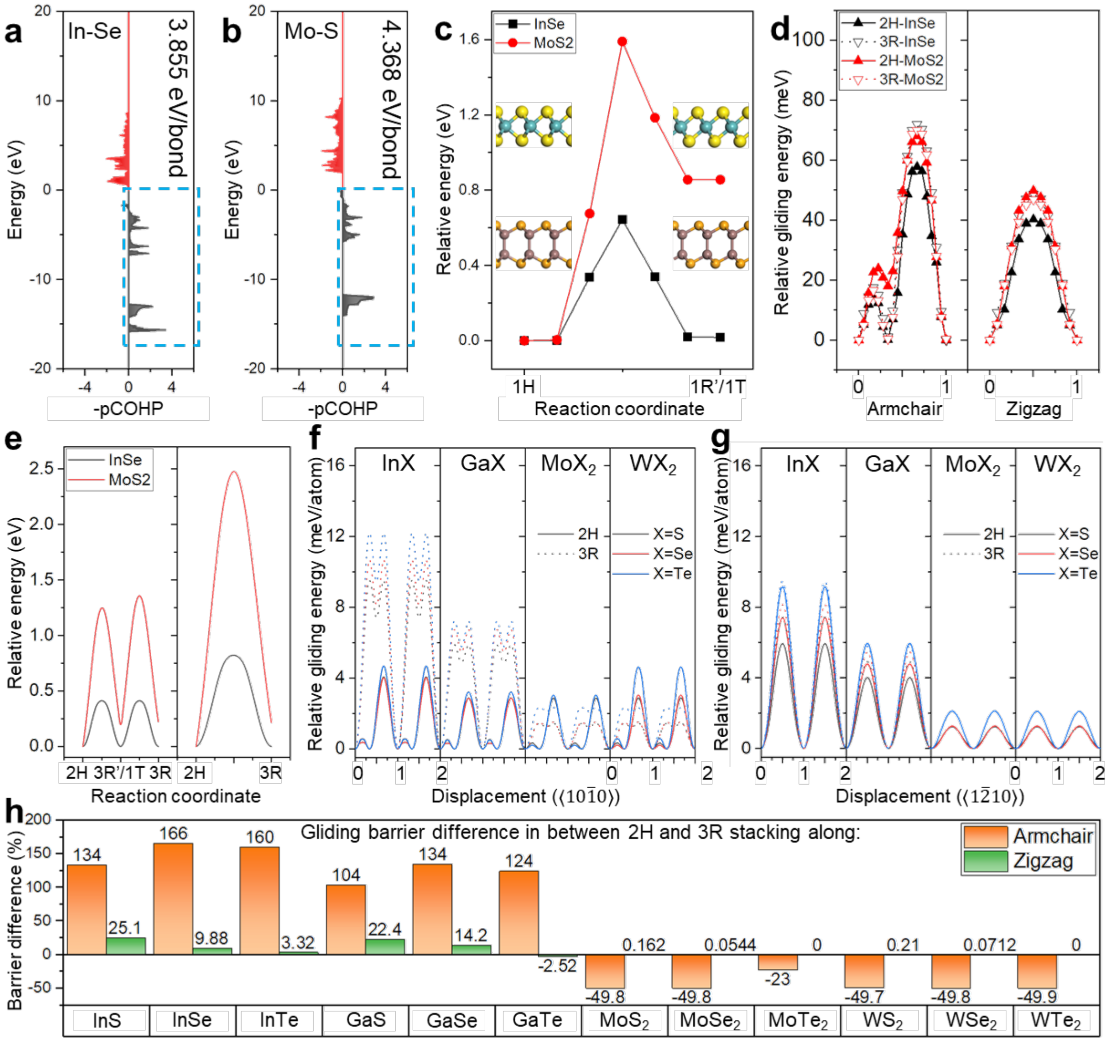

Fig. 5 | Theoretical calculations. a-d, First-principles calculations. Partial COHP for intralayer bonding of In-Se (**a**), and Mo-S (**b**). The integrated areas and the integrated bonding strengths are marked in the light blue dashed boxes (**a**,**b**). **c**, Phase transition energy barriers for 1L InSe (1H-to-1R') and MoS$_2$ (1H-to-1T) with schematics of the transition of chalcogen atoms. **d**, Gliding energy barriers along a period of armchair $\langle 10\bar{1}0\rangle$ and zigzag $\langle 1\bar{2}10\rangle$ for 2H and 3R phases InSe and MoS$_2$. **e-h,** LAMMPS simulations. **e,** Energy barriers of two-step and one-step phase transition for InSe (2H-to-3R'-to-3R) and MoS$_2$ (2H-to-1T-to-3R). **f,g,** Relative gliding energy per atom along two periods of armchair $\langle 10\bar{1}0\rangle$ (**f**) and zigzag $\langle 1\bar{2}10\rangle$ (**g**) for both 2H and 3R phases MX and MX$_2$. Solid and dotted line represent 2H and 3R phase, respectively, and black, red, and blue colors represent X = S, Se, Te, respectively in (**f&g**). Barrier values in (**f&g**) can be seen in Extended Data Table 2. **h**, A summary of gliding energy barrier summary of (**f&g**), where the change of gliding barrier along zigzag direction is unnoticeable for

MX_2.

According to Fig. 3a-h and Extended Data Figs. 6-8, the phase transition only occurs in MX but not in MX_2, as evidenced by the simultaneously observed 2H, 3R, and 3R′ phases near the phase boundary in the experiments. The observations suggest that 3R'-MX serves as the intermediate phase in the transition pathway in between 2H and 3R phases (Fig. 3f-h). Thus, the energy barrier of phase transition of 1L InSe (1H-to-1R') and MoS_2 (1H-to-1T) has been also calculated by first-principles calculations via climbing image nudged elastic band (CI-NEB), as shown in Fig. 5c. The calculated energy barrier for translating one X atom achieving the phase transition in 1L InSe (~0.644 eV) is much smaller than that in 1L MoS_2 (~1.590 eV). The transition of 1H-to-1R' is thermodynamically stable, and hence 3R stacking can be formed after repeating one more translation every even layer with interlayer gliding. However, the 1H-1T phase transition of MoS_2 is predicted as energy unfavorable transition. These results elucidate why we can observe phase transition in InSe but not in MoS_2 without thermal effect. As the present of 2H-to-3R phase transition, CI-NEB method was also used to examine the effect of phase transition and the plasticity by calculating the gliding energy of 2H and 3R phases for both InSe and MoS_2 (Fig. 5d, details see Supplementary Fig. S23). The gliding barrier of 3R-InSe increases obviously than that of 2H-InSe no matter gliding along a period of armchair $\langle 10\bar{1}0\rangle$ and zigzag $\langle 1\bar{2}10\rangle$ direction. On the contrary, the gliding barrier of 3R-MoS_2 is similar to the 2H-MoS_2. The increasing barrier can serve as a pinning point to cease the propagation of micro-cracks, and this is the reason why the InSe crystal generates micro-crack networks with tremendous nanometer scale microcracks (Extended Data Fig. 4b&Supplementary Figs. S3c-e).

Second, we have performed MD simulations to evaluate the energy barriers of phase transitions in representative InSe and MoS_2, as well as completed a comprehensive comparison of the interlayer gliding energies along the armchair and zigzag directions for InX, GaX, MoX_2, and WX_2 (X = S, Se, Te) of 2H and 3R phases at room temperature via 6L models. Fig. 5e displays the comparison between the two-step phase transition and one-step phase transition of InSe (2H-to-3R'-to-3R) and MoS_2 (2H-to-1T-to-3R) by translating the X atoms (details see Method). The results indicate the two-step phase transition only requires approximate half of the energy compared with the direct phase transition (Fig. 5e). After phase transition, another local minimum in InSe is observed which is close to the pristine pure 2H-stacking. In contrast, 1T and 3R in MoS_2 are energy unfavorable states and possess higher energy barrier compared with InSe, which are consistent with the first-principles calculations in Fig. 5c. This explains why the micro-cracks are surrounded by 3R phase in InSe and why MoS_2 is prone to fracture rather than undergoing phase transition under high strain (Figs. 2-3 and Extended Data Figs. 2-8). It is also in accordance with the absence of phase transition of MX_2 observed in our plastic deformation experiments.

Figs. 5f-h show the gliding energies along two energy favorable low index directions (armchair $\langle 10\bar{1}0\rangle$ and zigzag $\langle 1\bar{2}10\rangle$) for 2H and 3R stacking MX and MX_2 via translating 1 internal layer in the 6L models. In the 6L models, the results indicate that the $\langle 10\bar{1}0\rangle$ direction is more energetically favorable path for the interlayer gliding of MX before phase transition (gliding barriers are summarized in Extended Data Table 2). In contrast, gliding along $\langle 1\bar{2}10\rangle$ is more energy favorable in MX_2. In Figs. 5f&g, the solid and dotted lines represent 2H and 3R phase, respectively. On the other hand, the black, red, and blue lines represent X=S, Se, Te, respectively. The MD results have the similar prediction to the first-principles calculations that 3R-MX (M = In, Ga; X = S, Se, Te) have a much higher gliding barrier than 2H-MX, that increase over 100% along $\langle 10\bar{1}0\rangle$, and increase 3.32-25.1% along $\langle 1\bar{2}10\rangle$, except for GaTe, which has a slightly decrement along $\langle 1\bar{2}10\rangle$. In contrast, the gliding barriers of 3R-MX_2 (M = Mo, W; X = S, Se, Te) have a decrement as much as half along $\langle 10\bar{1}0\rangle$ compared with 2H-MX_2 and are almost the same as 2H-MX_2 along $\langle 1\bar{2}10\rangle$. Although there is no phase transition observed in post-deformed MX_2, the results still show the differences of gliding barrier in different phases between MX and MX_2, that suggests the gliding induced micro-cracks propagation can be ceased by the phase transition enhanced gliding barrier. Hence, even the phase transition occurs, the 3R stacking MoS_2 can only be rarely seen, because it is energy unfavorable and easily removed by further gliding. Among them, InSe has the largest gliding barrier increment that increases significantly ~166% along $\langle 10\bar{1}0\rangle$, followed by InTe, InS, GaSe, GaTe and InS. GaSe also shows the good deformability like InSe[8,25], with greater gliding barrier increment along $\langle 1\bar{2}10\rangle$, but slightly weaker mechanical performance. The results indicate the change of gliding barrier along $\langle 10\bar{1}0\rangle$ is a more important factor to determine the plasticity. This evidences that the gliding barrier rise caused by phase transition is beneficial to plasticity. Hence, we also predict other MX materials like InS, GaS, and InTe would also have a good plasticity.

The 2H and 3R phases for MX and MX_2 have very close thermodynamic energies, which means that 2H-MX is possibly transformed to 3R-MX and co-existed with 3R-MX under plastic deformation as observed in Fig. 3. However, the significant gliding energy increment in MX after 2H-to-3R transition plays an important role to suppress the gliding in the vicinal area of 3R phases (because the strain will be mostly carried by the easy gliding 2H phase area in MX), and the newly transformed 3R-MX can act as pinning points for the microcracks around. In this way, the phase transition in MX can cease or at least retard the micro-crack propagation and crack coalescence in MX. On the contrary, since MX_2 cannot transform from 2H to 3R under mechanical deformation and negatively increment of gliding the barrier, this additional "3R pinning" cannot benefit to the deformation of MX_2.

Thus, the microscopic secret for the avoidance of macroscopic fracture in MX materials can be briefly described as: 1) Abundant local phase transition areas result in interlayer stacking order change under large strain; 2) Micro-cracks are evenly generated at phase boundaries or defects to relax the strain; 3) Micro-crack areas with more interlayer gliding can further promote phase transition, and newly formed phases close to micro-cracks retard the interlayer gliding, hence ceasing micro-crack developing and coalescence; 4) A homogeneous strain relaxation is rendered by the micro-crack network and severe strain concentration is avoided.

Macroscopic view via elastic constants

After the microscopic investigation, we have also studied the mechanical properties by calculating the elastic constants of InSe and MoS_2. The calculated stiffness matrices of InSe and MoS_2 are summarized in Extended Data Table 3. The incompressibility along basal plane and out-of-plane can be estimated by C_{11} and C_{33}, which implies that the deformation would be harder in 2H-MoS_2 (C_{11} ≈ 231 GPa; C_{33} ≈ 46.4 GPa; $\varepsilon_{zz}@40MPa$ ≈ -48.1 %) compared with 2H-InSe (C_{11} ≈ 64.6 GPa; C_{33} = 34.1 GPa; $\varepsilon_{zz}@40MPa$ ≈ -59.5%) under the same mechanical deformation. This agrees with the results in Supplementary Fig. S1. The difference of the in-plane shear deformation between 3R-InSe, 2H-InSe and 2H-MoS_2 can be further seen from the calculated C_{66}, which are ~22.8, ~21.9 and ~88.0 GPa, respectively. The shear stiffness of out-of-plane C_{44} and in-plane C_{66} is increased by ~27% and ~4% after 2H-InSe transforms to 3R-InSe. This agrees with our experimental results and previous calculations, indicating that phase transition is beneficial to the plasticity. It also implies a higher possibility of the in-plane rotation in 2H-InSe compared with 2H-MoS_2, which means that the phase transition can be also caused by lattice rotation. However, the required energy of lattice rotation usually is much higher than the phase transition caused by chalcogen atom translation. Besides, the shear moduli of 2H-InSe and 2H-MoS_2 are 17.0 and 53.8 GPa, respectively. The lower shear moduli in InSe indicates that it is more easily deformed without structural failure in response to the shear deformation. Thus, from both microscopic- and macroscopic-view, InSe demonstrates better plasticity, as supported by the tensile strain test along basal plane results for InSe (~12%[7]) and MoS_2 (~9%[8]).

Discussions on the ultra-high plasticity

The previously overlooked gliding induced phase transition plays an important role in the ultra-high plasticity. In our two-step phase transition model, the intralayer 2H-to-3R'-to-3R phase transition of MX is an energetically favorable pathway to relax part of strain based on our observations and the theoretical calculations (Figs. 3&5 and Extended Data Fig. 10). Moreover, the phase boundary can be formed during the phase transition, which promotes strain concentration and thus the micro-cracks form. The propagation of micro-cracks is ceased by the starkly increasing gliding energy barrier of 3R-MX compared to original 2H-MX, suggesting that 3R phase serves as a pinning point during the deformation. Therefore, the concept of “2H gliding and 3R pinning” around the micro-cracks holds the key for the ultra-high plasticity of MX, especially for InSe. This is part of the reasons why the microscale intralayer cracks do not extend in z direction (vertical to the basal plane) or coalesce to form macroscopic fracture surfaces in MX. Other reasons that have been shown in the low magnification comparisons and the *in situ* bending experiments (Fig. 4&Extended Data Figs. 2-8). MX are prone to relax the strain by forming micro-cracks, phase transition and interlayer gliding. Even there are dislocations, the dislocations can be relaxed during deformation, as shown by our *in situ* TEM experiments.

The compression on the MX creates strain concentrated phase boundaries. Subsequently, large quantity of micro-cracks surrounded by mainly 3R regions in different layers and different locations allow for the reorganization of layers under compression or tensile strain, resulting in the ultra-plastic behavior. Those self-stabilized joints of 3R stacked micro-cracks not only avoids the complete fracture, but also forms micro-crack networks to strengthen the structure. At the end, we would like to use a scheme to summarize the mechanism of the plasticity in MX as shown in Fig. 6. In short, due to the synergetic effect of the micro-crack and the 3R pinning, MX can effectively avoid strain concentration till complete fracture.

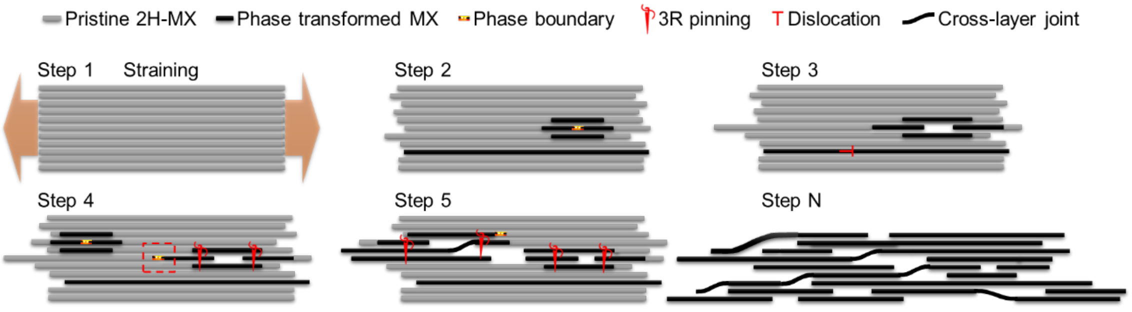

Fig. 6 | Schematics of the plastic deformation of MX materials.

In conclusion, we have discovered that the intralayer micro-cracks associated with 2H-to-3R’-to-3R phase transition of MX are essential for the strain relaxation and the ultra-high plastic behavior. The abundant well-organized micro-crack networks in MX crystals arise from the stark difference in gliding energy barrier between different phases/stacking orders, specifically 2H and 3R stackings. Due to the 3R pinning effect, the micro-cracks cannot coalesce or extend freely along z direction, but instead develop microscopic evenly distributed intralayer cracks, which eventually carry the ultra-high plastic strain via free-edge gliding and reorganization of fragmented layers. These new insights have clearly rationalized the superior plasticity in MX over other vdW-layered materials. These findings will open new directions for the mechanical engineering on the inorganic semiconducting crystals and will benefit the development of flexible electronic materials, advanced additive manufacturing on semiconductors, and solid-state lubricants. The unveiled novel plastic deformation mode facilitated by local phase transition and microcracks, which is entirely different from the conventional dislocation-carried or grain boundary-carried plasticity in crystals before, will potentially lead to a paradigm shift for designing ultrahigh plastic materials, especially for plastic inorganic semiconductors in the future.

Methods

Specimen preparations and experimental design

2H-InSe single crystal (size: 5×5 mm^2) was purchased from Nanjing Mukenano. 2H-GaSe (size: 7 mm), 2H-MoS_2 (size: 10 mm) and 2H-$MoTe_2$ (size: 10 mm) were purchased from HQ Graphene. Compression force was applied by PASCO ME-8236 with strain rate ~0.5/s until reaching the limitation of the machine (Supplementary Fig. S1), in order to create high density dislocations and micro-cracks. The size of the crystals was measured by a pair of digital calipers (±0.01 mm) and the thickness was measured by a micrometer (±5 μm). Some specimens were prepared by the hammer method under 2.45±0.01 N for 100~200 times until no obvious deformation was observed, that provides similar results to the compression machine. The compressed crystals were mechanically exfoliation by scotch tape and transferred by thermal release tape[47]. Pristine 2H crystals and post-deformed crystals were mechanically exfoliated without applying compress force and shear stress. The cross-section specimens were prepared by Helios 5 CX DualBeam focused ion beam (FIB) from the XRD tested crystals.

Characterizations

Atomic STEM images were acquired under a Cs-corrected STEM (Thermo Scientific^{TM} Spectra 300 (S)TEM operated at 300 kV with a convergence semi-angle of 24.4 mrad. The collection angles of HAADF detector were set as 35-200 mrad. The screen current was set as 10 pA by an unfiltered monochromator to reduce the irradiation damage. The TEM with selected area diffraction patterns (SAED) images were captured by Oneview charge-coupled device (CCD). During the in-situ experiments, TEM and STEM images were acquired by Orius SC1000 CCD and Digiscan II under a (S)TEM (JEOL JEM-2100F) operated at 200 kV.

Thickness estimation in STEM-HAADF

The line profiles with integration width 40 were extracted from GMS 3. The signal differences were confirmed by both STEM-HAADF and *in situ* TEM data, that corelates to the specimen thickness for thin specimens. The fitting of 15 adjacent-averaging points presented the extracted data points more understandable.

In situ TEM experiment

Nanofactory^{TM} holder has been implemented in JEM-2100F operated at 200 kV. Similar to our previous works[48], a homemade tungsten (W) tip was electrochemically etched for manipulating the specimen and a homemade TEM grid holder was used for the further characterization without damaging the TEM grid. The bending experiment was initiated by moving the W tip towards the InSe crystal via piezo-driven fine control. The bending process was video recorded in real time by Olympus Veleta CCD.

Molecular dynamics simulation

Large-scale Atomic/Molecular Massively Parallel Simulator (LAMMPS) (the version released on 29 September 2021)[49] has been performed to calculate the gliding barrier along $\langle 10\bar{1}0 \rangle$ and $\langle 1\bar{2}10 \rangle$ for 2H and 3R stacking order of MX (InS, InSe, InTe, GaS, GaSe and GaTe) and MX$_2$ (MoS$_2$, MoSe$_2$ MoTe$_2$, Ws$_2$, WSe$_2$ and WTe$_2$), as well as the phase transition barriers the representatives of MX and MX$_2$ (InSe and MoS$_2$) by using 6L models (details see Supplementary Fig. S24). The Stillinger-Weber potential[50] was used to approximate the intralayer interactions in MX and MX$_2$ and 12-6 Lennard-Jones potentials was used to approximate the non-bonded interlayer interactions. The cutoffs of Lennard-Jones potential were set 12.8 and 12.0 for MX and MX$_2$, respectively. All force-field parameters used in this work were taken from the previous study[51]. All modifications are applied under 300 K to simulate experimental environments. It should be noted the interlayer gliding is sometimes carried by dislocations, and the slight strain variation introduced by dislocations are ignored here, nevertheless, the extended widths of the interlayer dislocations in these vdW-layered materials greatly lower the strain level and will not influence the gliding barrier.

STEM-HAADF simulations

Dr. Probe[52] was used for simulating STEM-HAADF images. Accelerating voltage, convergence semi-angle, and collection angle were set same as the imaging, which were 300 kV, 24.4 mrad, and 35-200 mrad, respectively. Aberration correction values were set as following: A1: 1.84 nm (83.2°), A2: 13.5 nm (9.3°), B2: 30.7 nm (108.5°), C3: 252 nm, A3: 600 nm (-162°), S3: 216 nm (2.1°), A4: 3.31 µm (170.3°). 1L to 6L InSe simulations can be seen in Supplementary Fig. S25.

DFT calculations

Density functional theory (DFT) calculations were performed to study structural, electronic and mechanical properties of the vdW MX and MX$_2$ structures, in which Vienna Ab initio Simulation Package (VASP.6.3.0)[53,54] was used with a projector augmented wave (PAW)[55] basis and Perdew-Burke-Ernzerhof (PBE) parameterized Generalized Gradient Approximation (GGA) exchange-correlation functional. For all the calculations, the kinetic energy cutoff for electronic plane wave expansion was set to 400 eV. Γ-centered 12×12×2 and 1×12×2 *k*-pointsgrids were used to sample the first Brillouin zone of InSe and MoS_2 unit cell and supercell, respectively. Moreover, van der Waals interaction was considered using vdW-DF-cx method[56,57], which is better to reproduce experimental measured lattice constant and and elastic constant of InSe, compared with DFT+D2[58] and DFT+D3[59,60] (details see Supplementary Table S1&S2& Supplementary Note S1). The energy barrier of phase transition was calculated by the climbing image nudged elastic band (CI-NEB)[61] method using 10×1×3 supercell. Total energy and the forces on each atom were converged to less than 10^{-8} eV and 0.01 eV/Å, respectively. The elastic modulus of 2H and 3R phase of InSe and MoS_2 were calculated using a finite differences approach. The crystal orbital Hamilton populations (COHP) were calculated by LOBSTER package[62] to estimate the bond strength. The integration of partial COHP for bonding state (below Fermi level) was conducted to estimate the strength of In-Se and Mo-S bonding due to their same bonding configuration.

Mechanical properties from elastic constants

In generally, the stiffness tensor is denoted as following matrix,

$$C = \begin{bmatrix} C_{11} & C_{12} & C_{13} & C_{14} & C_{15} & C_{16} \\ C_{21} & C_{22} & C_{23} & C_{24} & C_{25} & C_{26} \\ C_{31} & C_{23} & C_{33} & C_{34} & C_{35} & C_{36} \\ C_{41} & C_{42} & C_{43} & C_{44} & C_{45} & C_{46} \\ C_{51} & C_{52} & C_{53} & C_{54} & C_{55} & C_{56} \\ C_{61} & C_{62} & C_{63} & C_{64} & C_{65} & C_{66} \end{bmatrix} \tag{1}$$

Considering the crystal symmetry of MoS_2 and InSe, we can simplify the matrix to be,

$$C = \begin{bmatrix} C_{11} & C_{12} & C_{13} & C_{14} & 0 & 0 \\ C_{12} & C_{11} & C_{13} & -C_{14} & 0 & 0 \\ C_{13} & C_{13} & C_{33} & 0 & 0 & 0 \\ C_{14} & -C_{14} & 0 & C_{44} & 0 & 0 \\ 0 & 0 & 0 & 0 & C_{44} & C_{14} \\ 0 & 0 & 0 & 0 & C_{14} & C_{66} \end{bmatrix} \tag{2}$$

Due to the anisotropic nature, Voigt-Reuss-Hill method is used to calculate the mechanical properties[63]. The bulk and shear moduli are denoted as,

$$B = 1/2(B_V + B_R) \tag{3}$$

$$G = 1/2(G_V + G_R) \tag{4}$$

where B_V and G_V are the Voigt bulk and shear moduli[64], and B_R and G_R are the Reuss bulk and shear moduli[65].

$$B_V = (2C_{11} + 2C_{12} + 4C_{13} + C_{33})/9 \tag{5}$$

$$G_V = (2C_{11} - C_{12} - 2C_{13} + C_{33} + 6C_{44} + 3C_{66})/15 \tag{6}$$

$$B_R = (2S_{11} + 2S_{12} + 4S_{13} + S_{33})^{-1} \tag{7}$$

$$G_R = 15/(8S_{11} - 4S_{12} - 8S_{13} - 4S_{33} + 6S_{44} + 3S_{66}) \tag{8}$$

where S_{ij} is the elastic compliances of C_{ij}. Then, the Young's modulus (E) and Poisson ratio (ν) are obtained.

$$E = 9BG/(3B + G) \tag{9}$$

$$\nu = (3B - 2G)/(6B + 2G) \tag{10}$$

The anisotropic index (A^L) is calculated by[66],

$$A^L = \sqrt{[ln(B_V/B_R)]^2 + 5[ln(G_V/G_R)]^2}$$

Raman Spectroscopy

Raman spectra were collected by the WITec Alpha300R confocal microscopy using a 532 nm laser with a grating of 1800 g/mm. The signals were collected under a 50X lens with the laser power of 0.5 mW and the integration time of 10 s.

X-Ray Diffraction

XRD spectra were conducted by the Rigaku SmartLab X-ray diffractometer with 9 kW rotating anode X-ray source (wavelength ≈ 1.54 Å).

References and notes

1 Petroski, H. M. C. The Pencil : a History of Design and Circumstance. (2011).

2 Kim, Y., Sung, A., Seo, Y., Hwang, S. & Kim, H. Measurement of hardness and friction properties of pencil leads for quantification of pencil hardness test. *Advances in Applied Ceramics* **115**, 443-448 (2016). https://doi.org:10.1080/17436753.2016.1186364

3 Heissenbüttel, M.-C., Marauhn, P., Deilmann, T., Krüger, P. & Rohlfing, M. Nature of the excited states of layered systems and molecular excimers: Exciplex states and their dependence on structure. *Physical Review B* **99**, 035425 (2019). https://doi.org:10.1103/PhysRevB.99.035425

4 Ermolaev, G. A. *et al.* Giant optical anisotropy in transition metal dichalcogenides for next-generation photonics. *Nature Communications* **12**, 854 (2021). https://doi.org:10.1038/s41467-021-21139-x

5 Nicolosi, V., Chhowalla, M., Kanatzidis, M. G., Strano, M. S. & Coleman, J. N. Liquid Exfoliation of Layered Materials. *Science* **340**, 1226419 (2013). https://doi.org:10.1126/science.1226419

6 Wang, Q. H., Kalantar-Zadeh, K., Kis, A., Coleman, J. N. & Strano, M. S. Electronics and optoelectronics of two-dimensional transition metal dichalcogenides. *Nature Nanotechnology* **7**, 699-712 (2012). https://doi.org:10.1038/nnano.2012.193

7 Wei, T. R. *et al.* Exceptional plasticity in the bulk single-crystalline van der Waals semiconductor InSe. *Science* **369**, 542-545 (2020). https://doi.org:10.1126/science.aba9778

8 Gao, Z. *et al.* High-throughput screening of 2D van der Waals crystals with plastic deformability. *Nature Communications* **13**, 7491 (2022). https://doi.org:10.1038/s41467-022-35229-x

9 Wang, Y., Szökölová, K., Nasir, M. Z. M., Sofer, Z. & Pumera, M. Electrochemistry of Layered Semiconducting AIIIBVI Chalcogenides: Indium Monochalcogenides (InS, InSe, InTe). *ChemCatChem* **11**, 2634-2642 (2019). https://doi.org:https://doi.org/10.1002/cctc.201900449

10 Luxa, J., Wang, Y., Sofer, Z. & Pumera, M. Layered Post-Transition-Metal Dichalcogenides (X−M−M−X) and Their Properties. *Chemistry – A European Journal* **22**, 18810-18816 (2016). https://doi.org:https://doi.org/10.1002/chem.201604168

11 Late, D. J. *et al.* GaS and GaSe Ultrathin Layer Transistors. *Advanced Materials* **24**, 3549-3554 (2012). https://doi.org:https://doi.org/10.1002/adma.201201361

12 Feng, W., Zheng, W., Cao, W. & Hu, P. Back gated multilayer InSe transistors with enhanced carrier mobilities via the suppression of carrier scattering from a dielectric interface. *Adv Mater* **26**, 6587-6593 (2014). https://doi.org:10.1002/adma.201402427

13 Wu, L. M. *et al.* InSe/hBN/graphite heterostructure for high-performance 2D electronics and flexible electronics. *Nano Research* **13**, 1127-1132 (2020).

https://doi.org:10.1007/s12274-020-2757-1

14 Jiang, J., Xu, L., Qiu, C. & Peng, L.-M. Ballistic two-dimensional InSe transistors. *Nature* (2023). https://doi.org:10.1038/s41586-023-05819-w

15 Yoon, Y., Ganapathi, K. & Salahuddin, S. How good can monolayer MoS_2 transistors be? *Nano Lett* **11**, 3768-3773 (2011). https://doi.org:10.1021/nl2018178

16 Radisavljevic, B. & Kis, A. Mobility engineering and a metal-insulator transition in monolayer MoS_2. *Nat Mater* **12**, 815-820 (2013). https://doi.org:10.1038/nmat3687

17 Zhong, F. *et al.* Substitutionally Doped $MoSe_2$ for High-Performance Electronics and Optoelectronics. *Small* **17**, 2102855 (2021). https://doi.org:https://doi.org/10.1002/smll.202102855

18 Cho, S. *et al.* Phase patterning for ohmic homojunction contact in $MoTe_2$. *Science* **349**, 625-628 (2015). https://doi.org:10.1126/science.aab3175

19 Wu, E. *et al.* Dynamically controllable polarity modulation of $MoTe_2$ field-effect transistors through ultraviolet light and electrostatic activation. *Science Advances* **5**, eaav3430 (2019). https://doi.org:10.1126/sciadv.aav3430

20 Fang, H. *et al.* High-Performance Single Layered WSe_2 p-FETs with Chemically Doped Contacts. *Nano Letters* **12**, 3788-3792 (2012). https://doi.org:10.1021/nl301702r

21 Iqbal, M. W. *et al.* High-mobility and air-stable single-layer WS_2 field-effect transistors sandwiched between chemical vapor deposition-grown hexagonal BN films. *Scientific Reports* **5**, 10699 (2015). https://doi.org:10.1038/srep10699

22 Wang, Y. *et al.* Electron mobility in monolayer WS_2 encapsulated in hexagonal boron-nitride. *Applied Physics Letters* **118**, 102105 (2021). https://doi.org:10.1063/5.0039766

23 Fu, D. *et al.* Tuning the electrical transport of type II Weyl semimetal WTe_2 nanodevices by Ga^+ ion implantation. *Scientific Reports* **7**, 12688 (2017). https://doi.org:10.1038/s41598-017-12865-8

24 Yan, Z. *et al.* Highly stretchable van der Waals thin films for adaptable and breathable electronic membranes. *Science* **375**, 852-859 (2022). https://doi.org:10.1126/science.abl8941

25 Wang, H. *et al.* Orientation-dependent large plasticity of single-crystalline gallium selenide. *Cell Reports Physical Science* **3**, 100816 (2022). https://doi.org:10.1016/j.xcrp.2022.100816

26 Qiu, D., Chu, Y., Zeng, H., Xu, H. & Dan, G. Stretchable MoS_2 Electromechanical Sensors with Ultrahigh Sensitivity and Large Detection Range for Skin-on Monitoring. *ACS Applied Materials & Interfaces* **11**, 37035-37042 (2019). https://doi.org:10.1021/acsami.9b11554

27 Sui, F. *et al.* Sliding ferroelectricity in van der Waals layered γ-InSe semiconductor. *Nature Communications* **14**, 36 (2023). https://doi.org:10.1038/s41467-022-35490-0

28 Rogée, L. *et al.* Ferroelectricity in untwisted heterobilayers of transition metal

dichalcogenides. *Science* **376**, 973-978 (2022). https://doi.org:10.1126/science.abm5734

29 El-Kady, M. F., Strong, V., Dubin, S. & Kaner, R. B. Laser Scribing of High-Performance and Flexible Graphene-Based Electrochemical Capacitors. *Science* **335**, 1326-1330 (2012). https://doi.org:10.1126/science.1216744

30 Vazirisereshk, M. R., Martini, A., Strubbe, D. A. & Baykara, M. Z. Solid Lubrication with MoS_2: A Review. *Lubricants* **7** (2019). https://doi.org:10.3390/lubricants7070057

31 Scharf, T. W. & Prasad, S. V. Solid lubricants: a review. *Journal of Materials Science* **48**, 511-531 (2013). https://doi.org:10.1007/s10853-012-7038-2

32 Berman, D., Erdemir, A. & Sumant, A. V. Graphene: a new emerging lubricant. *Materials Today* **17**, 31-42 (2014). https://doi.org:https://doi.org/10.1016/j.mattod.2013.12.003

33 Guo, Y. *et al.* Additive manufacturing of patterned 2D semiconductor through recyclable masked growth. *Proceedings of the National Academy of Sciences* **116**, 3437-3442 (2019). https://doi.org:10.1073/pnas.1816197116

34 Grubb, P. M., Subbaraman, H., Park, S., Akinwande, D. & Chen, R. T. Inkjet Printing of High Performance Transistors with Micron Order Chemically Set Gaps. *Scientific Reports* **7**, 1202 (2017). https://doi.org:10.1038/s41598-017-01391-2

35 Larson, N. M. *et al.* Rotational multimaterial printing of filaments with subvoxel control. *Nature* **613**, 682-688 (2023). https://doi.org:10.1038/s41586-022-05490-7

36 Berre, C. *et al.* Failure analysis of the effects of porosity in thermally oxidised nuclear graphite using finite element modelling. *Journal of Nuclear Materials* **381**, 1-8 (2008). https://doi.org:https://doi.org/10.1016/j.jnucmat.2008.07.021

37 Akimov, I. V., Sylovanyuk, V. P., Volchok, I. P. & Ivantyshyn, N. A. Influence of the shape of graphite inclusions on the mechanical properties of iron–carbon alloys. *Materials Science* **48**, 620-627 (2013). https://doi.org:10.1007/s11003-013-9546-x

38 Rudenko, A. N., Katsnelson, M. I. & Gornostyrev, Y. N. Dislocation structure and mobility in the layered semiconductor InSe: a first-principles study. *2D Materials* **8**, 045028 (2021). https://doi.org:10.1088/2053-1583/ac207b

39 Küpers, M. *et al.* Controlled Crystal Growth of Indium Selenide, In_2Se_3, and the Crystal Structures of α-In_2Se_3. *Inorganic Chemistry* **57**, 11775-11781 (2018). https://doi.org:10.1021/acs.inorgchem.8b01950

40 Grzonka, J., Claro, M. S., Molina-Sánchez, A., Sadewasser, S. & Ferreira, P. J. Novel Polymorph of GaSe. *Advanced Functional Materials* **31**, 2104965 (2021). https://doi.org:https://doi.org/10.1002/adfm.202104965

41 Hao, Q. *et al.* Phase Identification and Strong Second Harmonic Generation in Pure ε-InSe and Its Alloys. *Nano Letters* **19**, 2634-2640 (2019). https://doi.org:10.1021/acs.nanolett.9b00487

42 Sun, M. *et al.* ε-InSe single crystals grown by a horizontal gradient freeze method. *CrystEngComm* **22**, 7864-7869 (2020). https://doi.org:10.1039/D0CE01271H

43 Yu, W. J., Lau, W. M., Chan, S. P., Liu, Z. F. & Zheng, Q. Q. Ab initio study of phase transformations in boron nitride. *Physical Review B* **67**, 014108 (2003). https://doi.org:10.1103/PhysRevB.67.014108

44 Sachdev, H., Haubner, R., Nöth, H. & Lux, B. Investigation of the c-BN/h-BN phase transformation at normal pressure. *Diamond and Related Materials* **6**, 286-292 (1997). https://doi.org:https://doi.org/10.1016/S0925-9635(96)00697-8

45 Dutta, A., Reid, C. & Heinrich, H. Simulation of Incoherent Scattering in High-Angle Annular Dark-Field Scanning Electron Microscopy. *Microscopy and Microanalysis* **19**, 852-853 (2013). https://doi.org:10.1017/S1431927613006259

46 Ly, T. H. *et al.* Hyperdislocations in van der Waals Layered Materials. *Nano Letters* **16**, 7807-7813 (2016). https://doi.org:10.1021/acs.nanolett.6b04002

47 Caldwell, J. D. *et al.* Technique for the Dry Transfer of Epitaxial Graphene onto Arbitrary Substrates. *ACS Nano* **4**, 1108-1114 (2010). https://doi.org:10.1021/nn901585p

48 Wong, L.-W. *et al.* Site-specific electrical contacts with the two-dimensional materials. *Nature Communications* **11**, 3982 (2020). https://doi.org:10.1038/s41467-020-17784-3

49 Thompson, A. P. *et al.* LAMMPS - a flexible simulation tool for particle-based materials modeling at the atomic, meso, and continuum scales. *Computer Physics Communications* **271**, 108171 (2022). https://doi.org:10.1016/j.cpc.2021.108171

50 Jiang, J.-W. *Handbook of Stillinger-Weber Potential Parameters for Two-Dimensional Atomic Crystals*. (BoD–Books on Demand, 2017).

51 Rappe, A. K., Casewit, C. J., Colwell, K. S., Goddard, W. A. & Skiff, W. M. UFF, a full periodic table force field for molecular mechanics and molecular dynamics simulations. *Journal of the American Chemical Society* **114**, 10024-10035 (1992). https://doi.org:10.1021/ja00051a040

52 Barthel, J. Dr. Probe: A software for high-resolution STEM image simulation. *Ultramicroscopy* **193**, 1-11 (2018). https://doi.org:https://doi.org/10.1016/j.ultramic.2018.06.003

53 Kresse, G. & Furthmüller, J. Efficient iterative schemes for ab initio total-energy calculations using a plane-wave basis set. *Physical Review B* **54**, 11169-11186 (1996). https://doi.org:10.1103/PhysRevB.54.11169

54 Kresse, G. & Furthmüller, J. Efficiency of ab-initio total energy calculations for metals and semiconductors using a plane-wave basis set. *Computational Materials Science* **6**, 15-50 (1996). https://doi.org:https://doi.org/10.1016/0927-0256(96)00008-0

55 Blöchl, P. E. Projector augmented-wave method. *Physical Review B* **50**, 17953-17979 (1994). https://doi.org:10.1103/PhysRevB.50.17953

56 Dion, M., Rydberg, H., Schröder, E., Langreth, D. C. & Lundqvist, B. I. Van der Waals Density Functional for General Geometries. *Physical Review Letters* **92**, 246401 (2004). https://doi.org:10.1103/PhysRevLett.92.246401

57 Berland, K. & Hyldgaard, P. Exchange functional that tests the robustness of the plasmon description of the van der Waals density functional. *Physical Review B* **89**, 035412 (2014). https://doi.org:10.1103/PhysRevB.89.035412

58 Grimme, S. Semiempirical GGA-type density functional constructed with a long-range dispersion correction. *Journal of Computational Chemistry* **27**, 1787-1799 (2006). https://doi.org:https://doi.org/10.1002/jcc.20495

59 Grimme, S., Ehrlich, S. & Goerigk, L. Effect of the damping function in dispersion corrected density functional theory. *Journal of Computational Chemistry* **32**, 1456-1465 (2011). https://doi.org:https://doi.org/10.1002/jcc.21759

60 Grimme, S., Antony, J., Ehrlich, S. & Krieg, H. A consistent and accurate ab initio parametrization of density functional dispersion correction (DFT-D) for the 94 elements H-Pu. *The Journal of Chemical Physics* **132**, 154104 (2010). https://doi.org:10.1063/1.3382344

61 Henkelman, G., Uberuaga, B. P. & Jónsson, H. A climbing image nudged elastic band method for finding saddle points and minimum energy paths. *The Journal of Chemical Physics* **113**, 9901-9904 (2000). https://doi.org:10.1063/1.1329672

62 Nelson, R. *et al.* LOBSTER: Local orbital projections, atomic charges, and chemical-bonding analysis from projector-augmented-wave-based density-functional theory. *Journal of Computational Chemistry* **41**, 1931-1940 (2020). https://doi.org:https://doi.org/10.1002/jcc.26353

63 Hill, R. The elastic behaviour of a crystalline aggregate. *Proceedings of the Physical Society. Section A* **65**, 349 (1952).

64 Voigt, W. Lehrbuch der Kristallphysik (Textbook of crystal physics). *BG Teubner, Leipzig und Berlin* (1928).

65 Reuss, A. Calculation of the flow limits of mixed crystals on the basis of the plasticity of monocrystals. *Z. Angew. Math. Mech* **9**, 49-58 (1929).

66 Kube, C. M. Elastic anisotropy of crystals. *AIP Advances* **6**, 095209 (2016). https://doi.org:10.1063/1.4962996

Acknowledgements

This work was supported by National Natural Science Foundation of China (Grant Nos. 52173230, 52222218, 52272045), Hong Kong Research Grant Council Collaborative Research Fund (Project No. C5029-18E), the Hong Kong Research Grant Council General Research Fund (Project No. 15301623, 11312022, 15302522, 11300820, 15302419), the City University of Hong Kong (Project No. 6000758, 9211308, 9667223, 9678303), The Hong Kong Polytechnic University (Project Nos. ZVGH, 1-BE47, ZE0C, and ZE2F), Environment and Conservation Fund (Project No. 69/2021, 34/2022), the Shenzhen Science, Technology and Innovation Commission (Project No. JCYJ20200109110213442), The State Key Laboratory of Marine Pollution (SKLMP) Seed Collaborative Research Fund SKLMP/SCRF/0037, The Research Institute for Advanced Manufacturing of The Hong Kong Polytechnic University.

Author information

Authors and Affiliations

Department of Applied Physics, The Hong Kong Polytechnic University, Kowloon, Hong Kong, China

Lok Wing Wong, Ke Yang, Wei Han, Xiaodong Zheng, Hok Yin Wong, Chi Shing Tsang, Shu Ping Lau, Ming Yang & Jiong Zhao

Polytechnic University of Hong Kong Shenzhen Research Institute, Shenzhen, China.

Lok Wing Wong, Xiaodong Zheng, Ming Yang & Jiong Zhao

Department of Chemistry and Center of Super-Diamond & Advanced Films (COSDAF), City University of Hong Kong, Kowloon, Hong Kong, China

Chun-Sing Lee, Thuc Hue Ly

Department of Chemistry and State Key Laboratory of Marine Pollution, City University of Hong Kong, Hong Kong, China

Thuc Hue Ly

City University of Hong Kong Shenzhen Research Institute, Shenzhen, China

Thuc Hue Ly

Contributions

J.Z., M.Y., T.H.L. led and supervised this project. L.W.W. planned the project, wrote the original manuscript, and conducted FIB, STEM-HAADF, *in situ* TEM, MD simulations, and STEM simulations. H.W., X.Z., C.S.L., S.P.L., T.H.L. and J.Z. helped data analysis. L.W.W. and W.H. prepared the materials. L.W.W., W.H. and H.Y.W. contributed to the XRD. L.W.W., W.H. and C.S.T. collected Raman data. K.Y. and M.Y. calculated the DFT results. All authors read and approved the manuscript. Reprints and permissions information is available at www.nature.com/reprints.

Corresponding author

Correspondence to Jiong Zhao or Ming Yang or Thuc Hue Ly.

Ethics declarations

Competing interests

The authors declare no financial or non-financial conflicts of interest.

Peer review

Peer review information

Nature Materials thanks XXXXXX, reviewer(s) for their contribution to the peer review of this work.

Additional Information

Publisher's note Springer Nature remains neutral with regard to jurisdictional claims in published maps and institutional affiliations.

Extended Data Information is available for this paper. Correspondence and requests for materials should be addressed to J.Z. (jiongzhao@polyu.edu.hk), M.Y. (kevin.m.yang@polyu.edu.hk), or T.H.L. (thuchly@cityu.edu.hk).

Reprints and permissions

Extended Data Figures and Tables

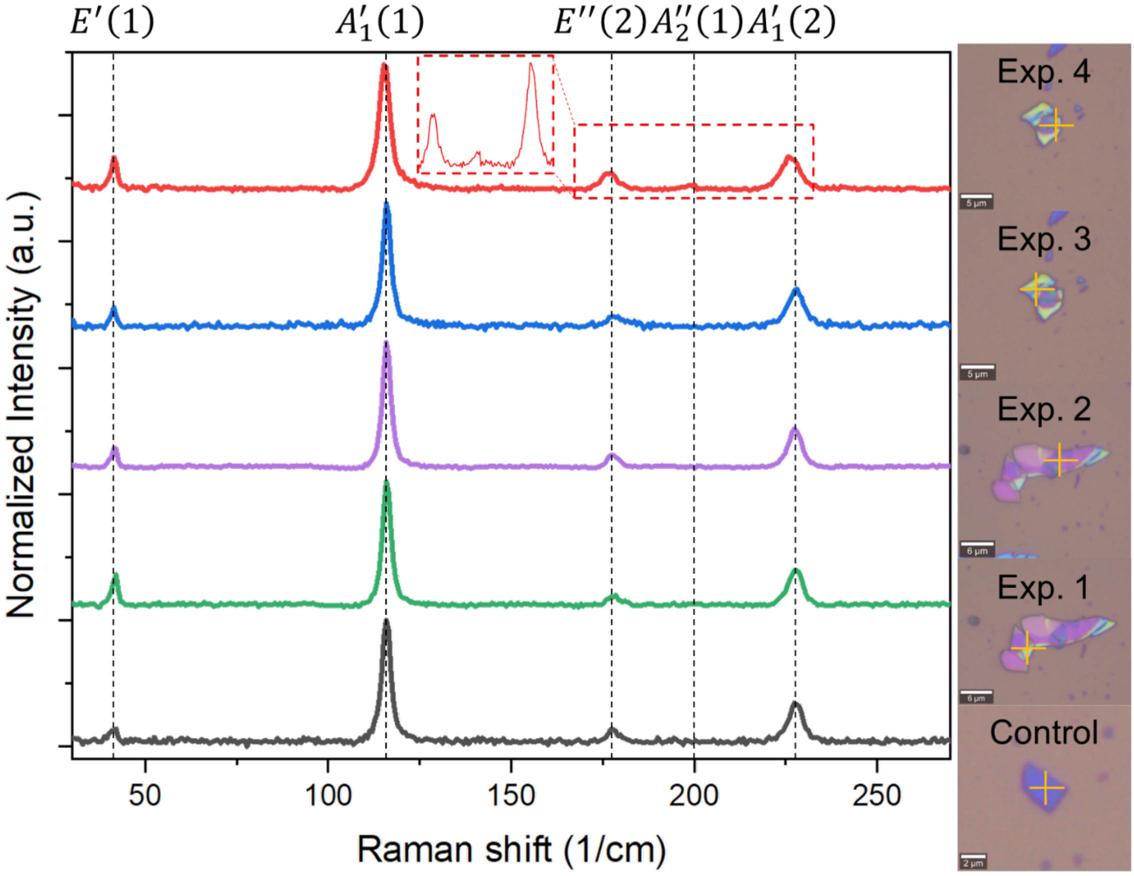

Peak (1/cm)	41	116	178	199	227
Exp. 4	26.6	100	14.2	4.80	26.9
Exp. 3	17.8	100	10.7	0	32.5
Exp. 2	15.8	100	10.8	0	31.8
Exp. 1	26.0	100	9.89	0	29.4
Control	14.0	100	13.9	0	34.6

Extended Data Fig. 1 | Raman spectra with corresponding optical images and a table of normalized peak intensity (%). The orange crosses in the optical images indicate the laser excited position. The post-deformed InSe presents stronger E’(1) and weaker E”(2), representing 3R stacking. Exp. 4 displays a red shift with an extra peak at 199 cm^{-1} that attributes to some local 2R phase.

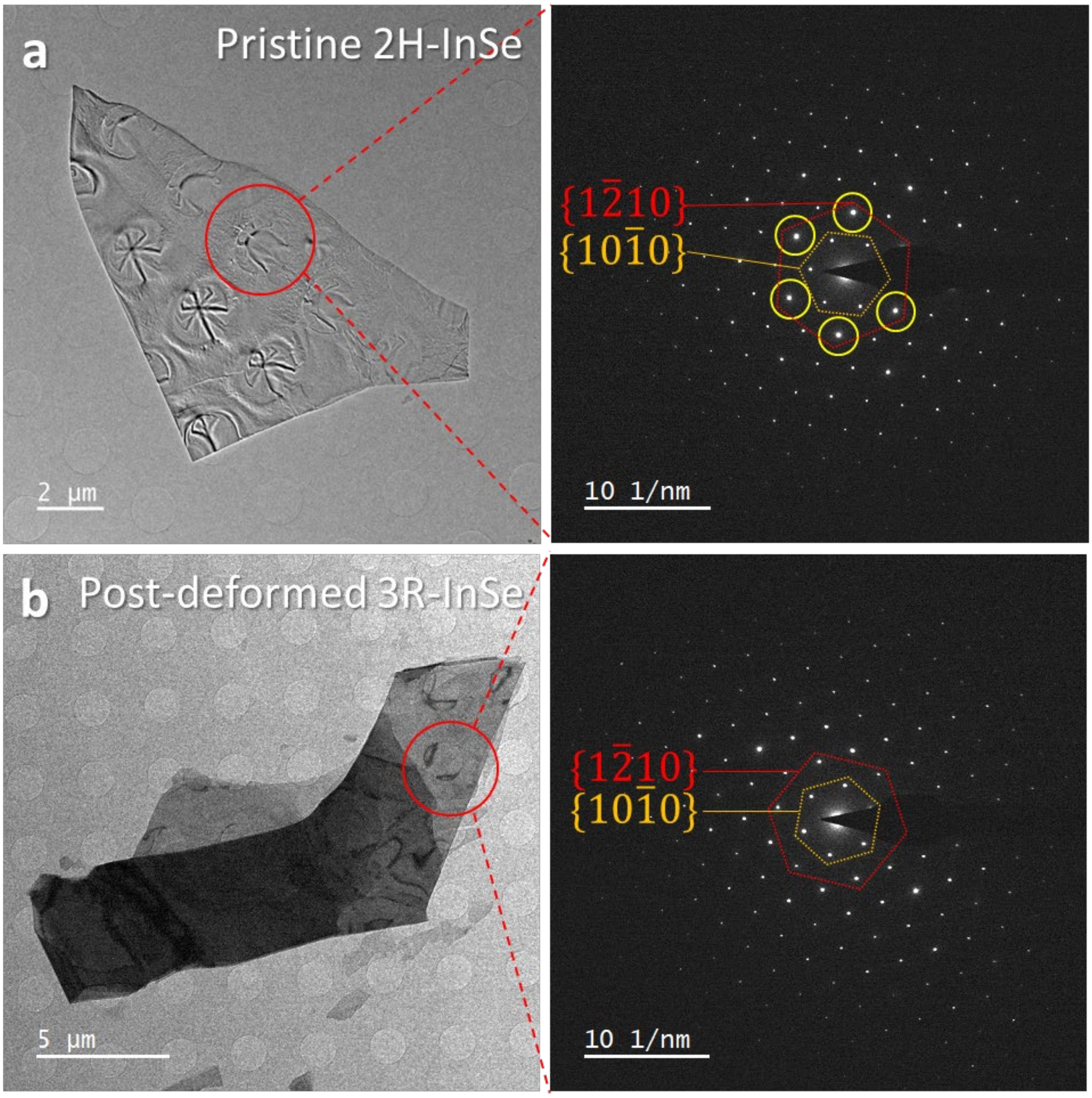

Extended Data Fig. 2 | Low magnification TEM top views with selected area diffraction patterns (SAED). **a,** Pristine InSe. **b,** Post-deformation InSe. Red circles show the selected area. Yellow circles in (**a**) highlight the stronger diffraction signal of $\{1\bar{2}10\}$ of the pristine 2H-InSe.

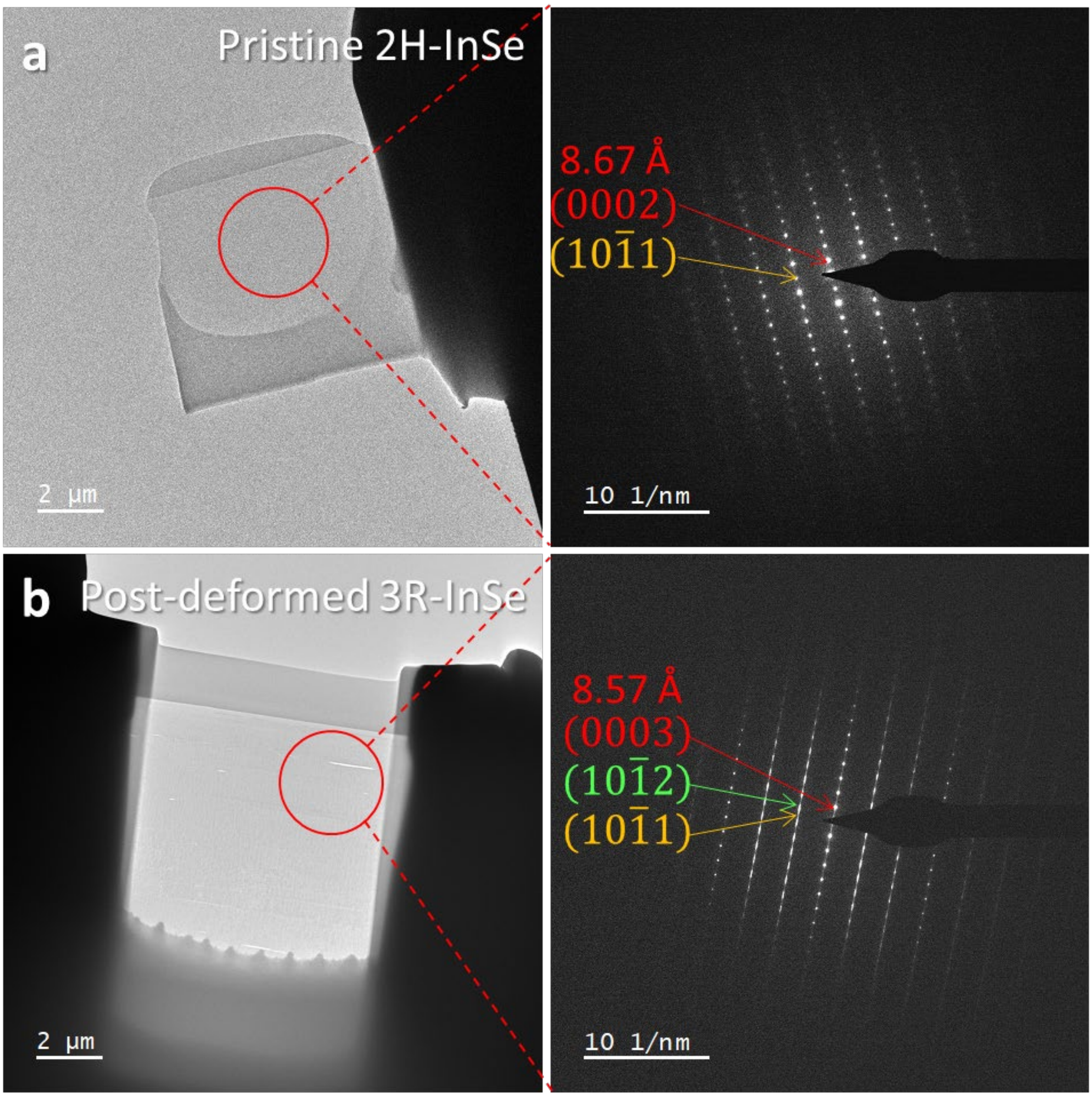

Extended Data Fig. 3 | Low magnification TEM cross-section views with SAED. a, Pristine InSe. **b,** Post-deformation InSe. Red circles show the corresponding selected area. The average interlayer spacing is slightly shorter after deformation.

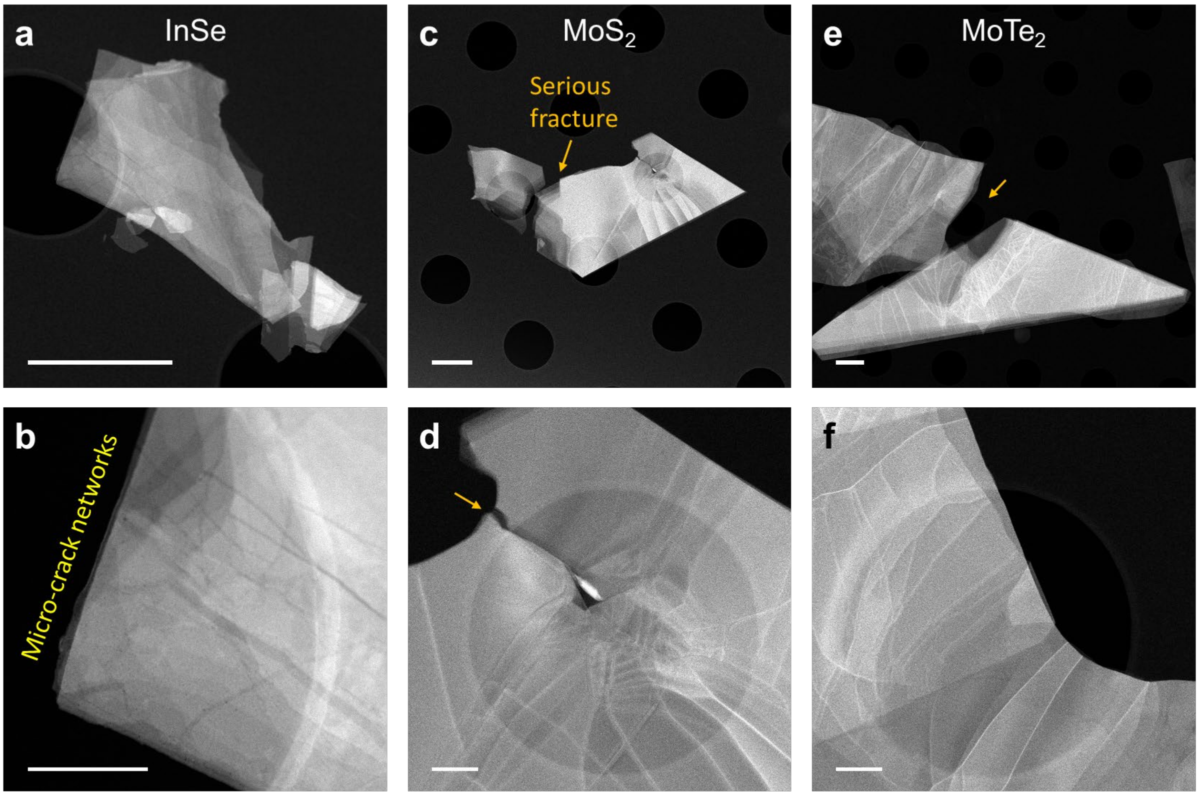

Extended Data Fig. 4 | Top views of typical of low magnification STEM-HAADF after deformations. a-f, InSe (**a**,**b**), MoS$_2$ (**c**,**d**), and MoTe$_2$ (**e**,**f**). Scale bars: 1 µm (**a**,**c**,**e**) and 200 nm (**b**,**d**,**f**). The orange arrows denote the serious fractures. InSe prefers relaxing strain by forming discrete micro-cracks, while MoS$_2$ and MoTe$_2$ prefer storing strain by dislocations, hence forming serious fracture eventually.

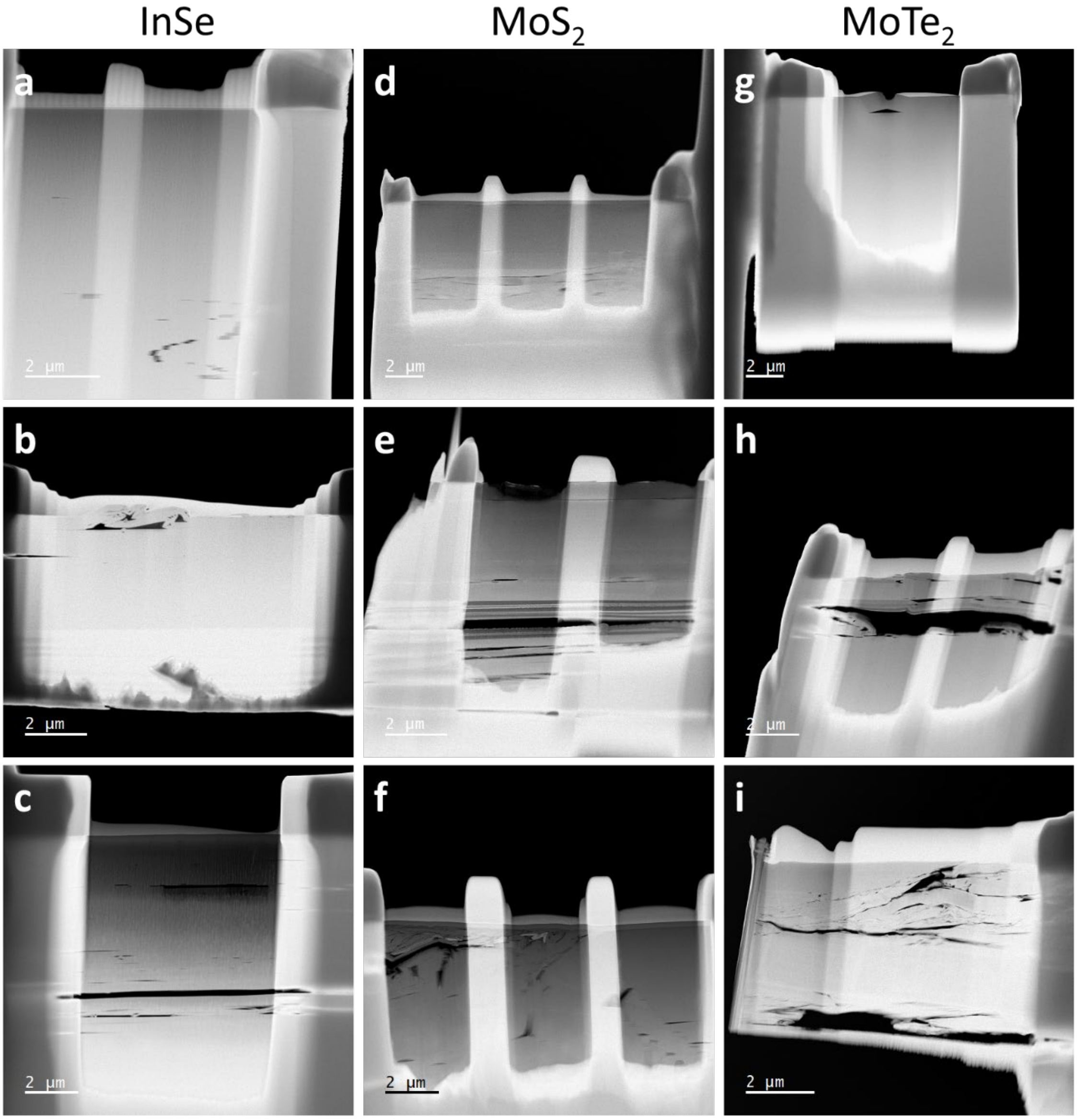

Extended Data Fig. 5 | Cross-section view of typical low magnification STEM-HAADF after deformations. **a-i,** InSe (**a-c**), MoS$_2$ (**d-f**), and MoTe$_2$ (**g-i**). InSe has significantly fewer large cracks than MoS$_2$ and MoTe$_2$. Scale bars: 2 μm (**a-i**).

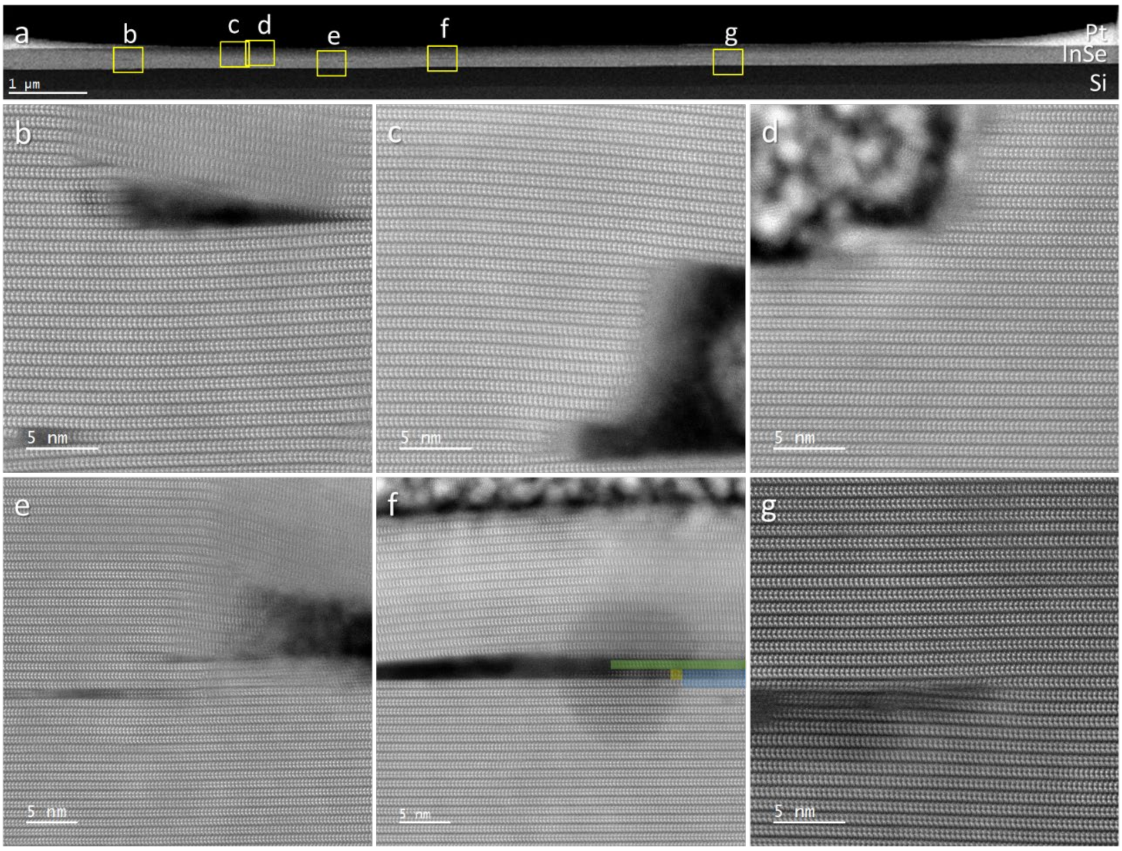

Extended Data Fig. 6 | Cross-section views of post-deformation InSe near micro-cracks. a, Full field of view of the post-deformed InSe supported by Si substrate. **b-g**, Corresponding atomic resolution STEM-HAADF highlighted by yellow boxes in (**a**). The grey scale (almost all the viewing area) represents 3R stacking while green, yellow, and blue in (**f**) highlight 3R' stacking, phase boundary, and 2H stacking, respectively.

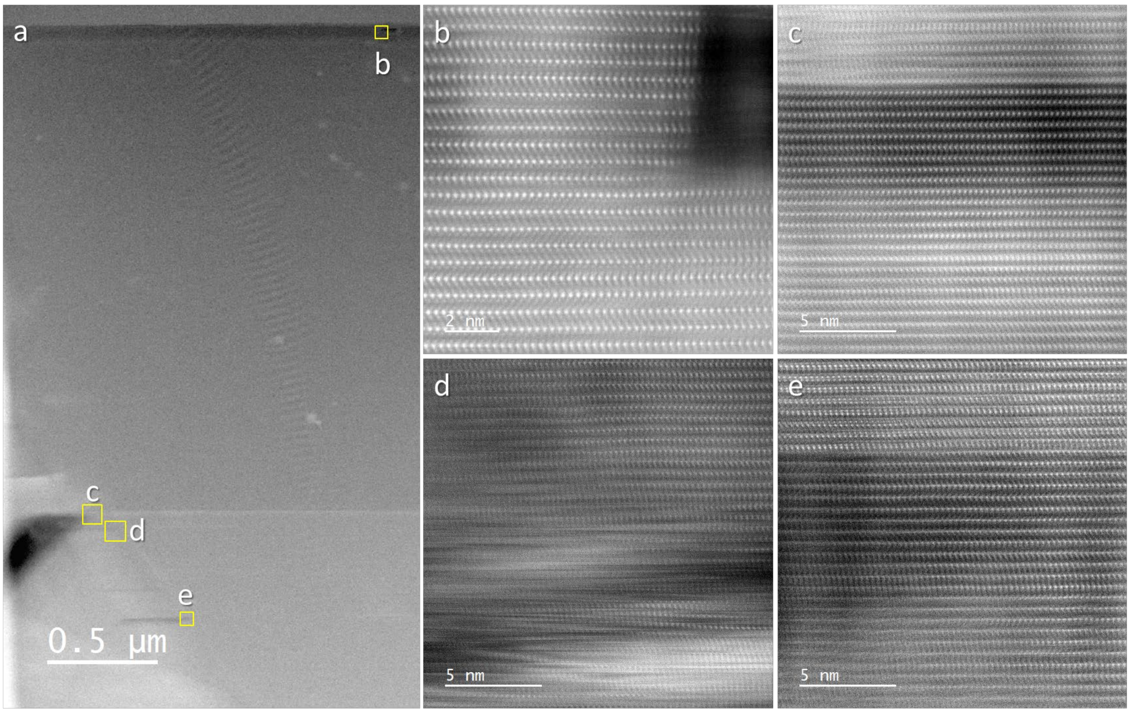

Extended Data Fig. 7 | Atomic cross-section views of the post-deformed MoS_2 near micro-cracks and defects. **a**, The large field of view of the experimental $MoTe_2$. **b-e**, Corresponding atomic resolution HAADF-STEM highlighted by yellow boxes in **a**, showing well 2H stacking. All the region demonstrates 2H stacking in MoS_2 after deformation.

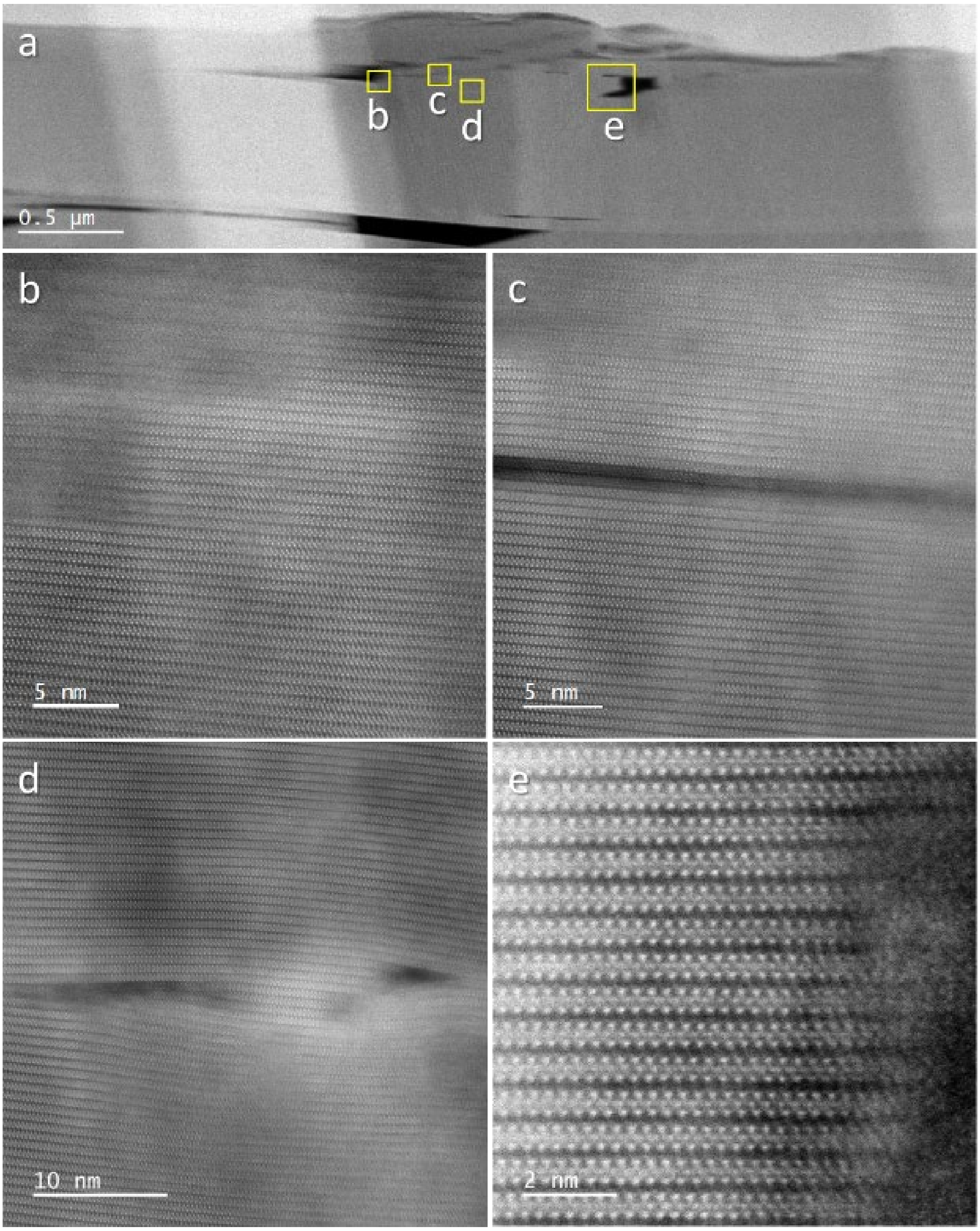

Extended Data Fig. 8 | Atomic cross-section views of the post-deformed $MoTe_2$ near micro-cracks and defects. a, The large field of view of the experimental $MoTe_2$. **b-e**, Corresponding atomic resolution HAADF-STEM highlighted by yellow boxes in **a**, showing well 2H stacking. All the region demonstrates 2H stacking in $MoTe_2$ after deformation.

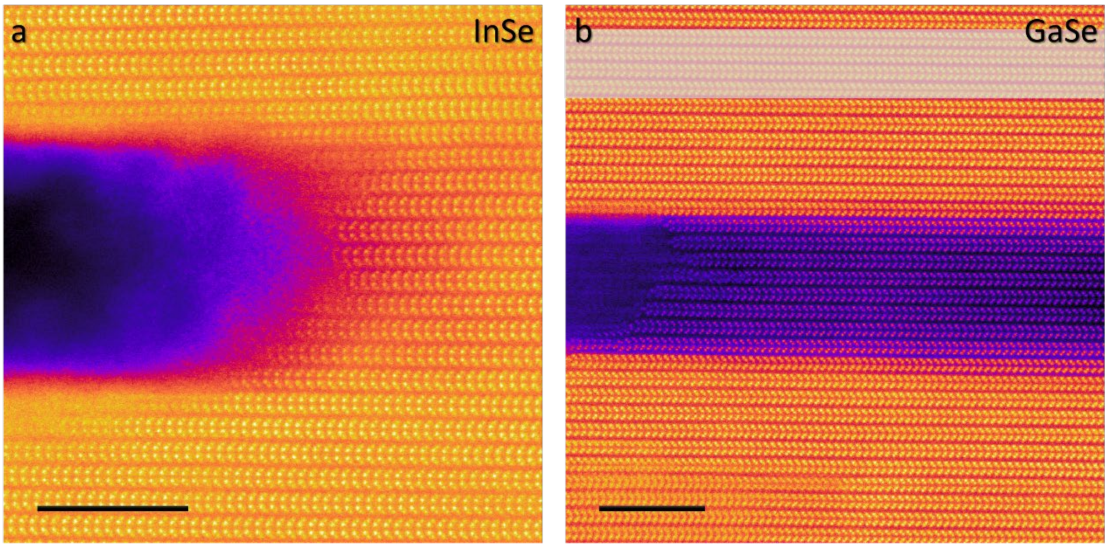

Extended Data Fig. 9 | Cross-section views of the typical multilayer micro-cracks. a, InSe. **b,** GaSe. Scale bars: 5 nm. The stacking near the few layers micro-cracks is mainly 3R stacking. The untransformed 2H stacking is highlighted in white in (**b**).

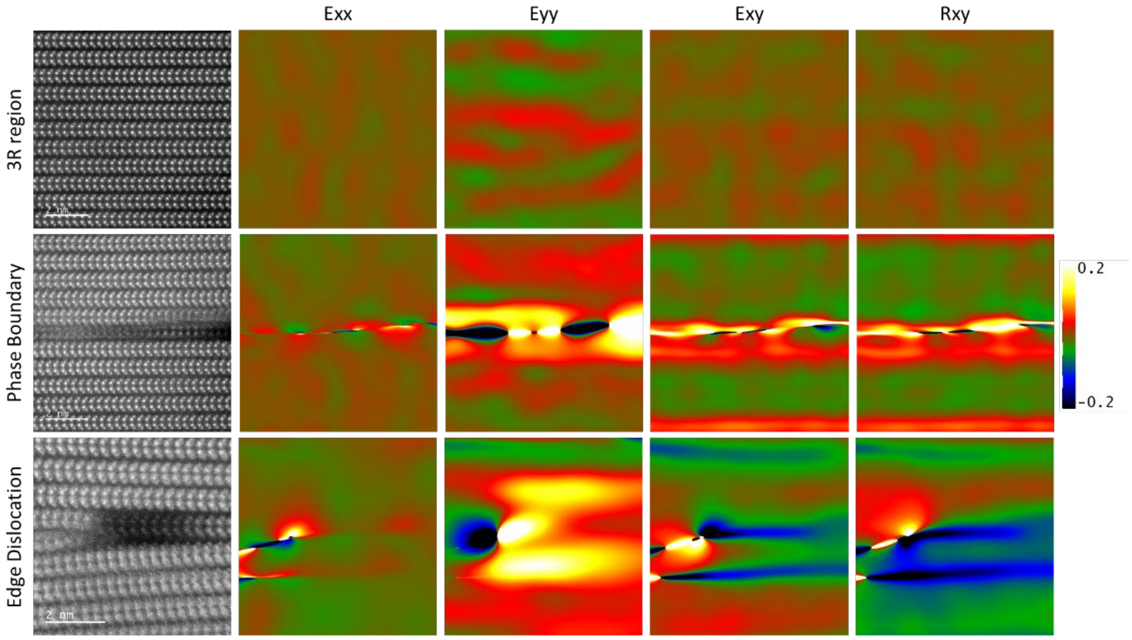

Extended Data Fig. 10 | Strain analysis by geometric phase analysis of completely transformed 3R region, phase boundary and edge dislocation. Scale bars: 2 nm. The 3R region after phase transition demonstrates strain relaxation, while the phase boundary and edge dislocation regions show strain concentration.

Extended Data Table 1 | Exfoliation energy and formation energy

	Exfoliation energy (J/m^2)	**Formation energy (eV/atom)**
3R-InSe	0.29	-0.756
2H-InSe	0.27	-0.755
2H-MoS_2	0.40	-1.212

Extended Data Table 2 | Gliding barrier per atom along armchair $\langle 10\bar{1}0\rangle$ and zigzag $\langle 1\bar{2}10\rangle$ directions

	$\langle 10\bar{1}0\rangle$ $(meV/atom)$			$\langle 1\bar{2}10\rangle$ $(meV/atom)$		
	2H	**3R**	**%diff.**	**2H**	**3R**	**%diff.**
InS	4.071	9.520	133.8	5.939	7.430	25.09
InSe	4.023	10.682	165.5	7.416	8.148	9.876
InTe	4.686	12.203	160.4	9.164	9.468	3.320
GaS	2.885	5.883	103.9	4.014	4.914	22.41
GaSe	2.873	6.736	134.5	4.789	5.471	14.23
GaTe	3.214	7.213	124.4	5.951	5.801	-2.525
MoS_2	2.874	1.444	-49.78	1.236	1.238	0.162
$MoSe_2$	3.040	1.526	-49.81	1.276	1.277	0.054
$MoTe_2$	3.040	2.341	-22.99	2.133	2.133	0.000
WS_2	2.881	1.449	-49.70	1.240	1.243	0.210
WSe_2	3.045	1.530	-49.76	1.280	1.281	0.071
WTe_2	4.637	2.325	-49.86	2.122	2.122	0.000

Extended Data Table 3 | DFT calculated elastic constants (C_{ij}), bulk modulus (B), shear modulus (G), Young's modulus (E), Poisson ratio (ν), and Anisotropy index (A^L) of 3R-InSe, 2H-InSe, and 2H-MoS_2

Materials	**3R-InSe**	**2H-InSe**	**2H-MoS_2**
C_{11} (GPa)	68.2490	64.5820	230.8140
C_{12} (GPa)	22.5560	21.1160	54.8430
C_{13} (GPa)	14.1800	10.9123	8.3180
C_{14} (GPa)	3.5560	0.0000	0.0000
C_{33} (GPa)	36.1030	34.0661	46.4350
C_{44} (GPa)	11.9930	9.4168	20.5580
C_{66} (GPa)	22.8460	21.9333	87.9860
B (GPa)	28.776	26.007	55.177
G (GPa)	18.901	16.993	53.765
E (GPa)	46.518	41.861	121.75
ν	0.2306	0.2317	0.1322
A^L	0.3576	0.2514	0.6504